

Deconfinement transition and localization of Dirac modes in finite-temperature \mathbb{Z}_3 gauge theory on the lattice

György Baranka* and Matteo Giordano†

*ELTE Eötvös Loránd University, Institute for Theoretical Physics,
Pázmány Péter sétány 1/A, H-1117, Budapest, Hungary*

We study the localization properties of the eigenmodes of the staggered Dirac operator across the deconfinement transition in finite-temperature \mathbb{Z}_3 pure gauge theory on the lattice in 2+1 dimensions. This allows for nontrivial tests of the sea-islands picture of localization, according to which low modes should localize on favorable Polyakov-loop fluctuations in the deconfined phase of a gauge theory. We observe localized low modes in the deconfined phase of the theory, both in the real Polyakov-loop sector, where they are expected, and in the complex Polyakov-loop sectors, where they are not. Our findings expose the limitations of the standard sea-islands picture, and call for its refinement. An improved picture, where spatial hopping terms play a more prominent role, is proposed and found to be in excellent agreement with numerical results.

I. INTRODUCTION

Confinement of static color charges is one of the most striking features of pure gauge theories, present at zero and low temperatures for a large variety of gauge groups. While an analytic understanding is still largely incomplete, this phenomenon has been convincingly demonstrated by means of numerical simulations in lattice gauge theory. However, the general mechanism of confinement, and of the deconfinement transition observed at finite temperature, is still the object of active research. A relatively recent approach to this issue is through the study of the localization properties of the eigenmodes of the Dirac operator, which are closely related to the confining properties of the theory (see Ref. [1] for a recent review). In all the pure gauge theories examined so far, all displaying an exact center symmetry, it was found that localized modes are absent in the low temperature, confined phase, and present in the high temperature, deconfined phase when the trivial Polyakov-loop sector is selected, appearing exactly at the deconfinement transition (within numerical errors) [2–12]. The connection between localization and deconfinement has been demonstrated also in the presence of fermions, when a sharp transition is present [13, 14]. Most interestingly, this connection has been demonstrated, albeit in a weaker sense, also in real-world QCD where the transition is only a crossover, with localized modes appearing in the temperature range where both confining and chiral properties of the theory change rapidly [15–19]. Here localization of the low modes could be the link that ties these properties together, providing a mechanism that explains the improvement of the chiral symmetry properties generally observed at deconfinement in gauge theories with fermions (e.g., through the reduction of the chiral condensate).

A qualitative understanding of the close relationship

between localization and deconfinement has been suggested in Ref. [7] and further developed in Refs. [1, 20–22], and is referred to as the “sea-islands picture” of localization. In this picture, the localization of Dirac eigenmodes is explained in terms of two features: (1) the presence in the high-temperature phase of a “sea” of ordered local Polyakov loops that get close to 1 in the physical, real center sector selected by fermions and (2) the presence of “islands” of Polyakov-loop fluctuations away from the ordered value. The main effect of Polyakov-loop ordering, combined with the twist imposed on fermion wave functions by the antiperiodic temporal boundary condition, is to open a “pseudogap” in the spectral density of the Dirac operator, driven by the lowest Matsubara frequency. The effect of a nontrivial Polyakov-loop fluctuation is to effectively and locally reduce the temporal twist on the fermion wave function, and for modes localized on the fluctuation this is expected to lower the eigenvalue below the lowest Matsubara frequency, if the spatial hopping terms do not offset the gain. As long as this is the case, it is then “energetically” convenient for the eigenmodes to localize on islands of fluctuations, leading to populating the pseudogap with a relatively low density of modes.

The sea-islands picture leads one to expect localized low modes in the deconfined phase of a generic gauge theory where Polyakov loops get ordered near the trivial value, independently of the gauge group and of the dimensionality of the system. Such an expectation is supported by numerical results covering a wide variety of gauge theories [1–13, 15–19] and related models [20–23]. The observed correlation between localized modes and Polyakov-loop fluctuations supports the mechanism outlined above [7, 12, 18, 19]. These studies include also the simplest theory displaying a deconfinement transition, i.e., \mathbb{Z}_2 gauge theory in 2+1 dimensions, investigated by us in Ref. [12]. The study of the simplest gauge models can provide valuable information on the mechanisms underlying localization, since in these models many features that should be irrelevant to localization but could confuse the picture are simply absent.

* barankagy@caesar.elte.hu

† giordano@bodri.elte.hu

One should mention at this point that a second localization mechanism is available for topologically non-trivial gauge groups. In this case one expects to find near-zero modes of topological nature, originating from the exact zero modes supported by isolated calorons and anti-calorons. Since at high temperature (anti)calorons form a dilute medium, the corresponding zero-modes can mix little with each other (as well as with delocalized modes that are well separated in energy, living beyond the pseudogap), and so topological near-zero modes are expected to be localized (see Refs. [24, 25]). A peak of localized near-zero modes has been indeed observed in the spectral density in SU(3) gauge theory in 3+1 dimensions [26]. (See, however, also Refs. [27, 28] for a different point of view on the behavior of the lowest, almost-zero modes.) A similar peak is present also in QCD with near-physical and lower-than-physical quark masses [17, 29–31], and there are indications that these modes are localized [17], which could have interesting consequences if the peak survives the chiral limit [32–34]. In spite of appearance, this mechanism is not in contrast with the sea-islands picture, since the Polyakov loop is non-trivial near (anti)calorons, but complements it by indicating a source of favorable Polyakov-loop fluctuations when there is non-trivial topology. On the other hand, localization has been observed also when topology is trivial; even when it is non-trivial, topological fluctuations are not sufficient to account for all the localized modes [7, 35]. The sea-islands mechanism then appears to be more fundamental.

The sea-islands picture can be extended to the case where a nontrivial Polyakov-loop sector is selected in the deconfined phase, provided one takes into account that here the ordered Polyakov loop does not correspond to the maximal possible twist for the fermions. This leads to a variety of scenarios. For example, if Polyakov loops get ordered near -1 , as may be the case, e.g., in SU($2N$) or \mathbb{Z}_{2N} theories, then localization of low modes is not expected, since the ordered loops already correspond to the most favorable places, where the twist on the fermion wave function is completely offset by the Polyakov loop, and all fluctuations correspond to a non-vanishing twist. This has been verified in 2+1 dimensional \mathbb{Z}_2 gauge theory [12]. For QCD at imaginary chemical potential $\mu_I = \pi T$, one of the complex Polyakov-loop sectors $e^{\pm i \frac{2\pi}{3}}$ is selected above the deconfinement (Roberge-Weiss) temperature, and local fluctuations to the real sector reduce the twist on the fermion wave function. This leads one to expect localization of the low modes, that has been observed in Ref. [14].

In this context, a particularly interesting setup is the deconfined phase of \mathbb{Z}_N theories with N odd, when Polyakov loops get ordered near $-e^{\mp i \frac{\pi}{N}}$. In this case one finds again that the sea of ordered loops corresponds to the most favorable twist on the fermion wave function. At best, islands of fluctuations where the Polyakov loop takes the value $-e^{\pm i \frac{\pi}{N}}$ can provide an equally but not more convenient twist, and so one is led to expect

delocalized low modes. Finding localized modes instead would pose a challenge to the standard sea-islands picture of localization, and would require the effect of spatial hopping terms in the staggered operator to be favorable to localization, contrary to what one would naively expect.

In this paper we continue our study of localization of the low Dirac modes and of the sea-islands picture investigating the second simplest gauge theory with a deconfining phase transition, namely lattice \mathbb{Z}_3 gauge theory in 2+1 dimensions, that we probe with the staggered Dirac operator. There is a number of features that make this model interesting. The most evident one is that since \mathbb{Z}_3 is the center of SU(3), which is the gauge group of QCD, any insight obtained here could be useful to better understand the physically relevant case. A less evident feature is that \mathbb{Z}_3 is the Abelian group where the standard sea-islands picture in the trivial Polyakov-loop sector has the largest chance to fail. In fact, the maximal possible gain in temporal twist provided by a Polyakov loop fluctuating to one of the complex, non-trivial sectors in a sea of trivial Polyakov loops is here at its lowest, and the effect of the spatial hopping terms might prevent localization. The least evident and most interesting feature is that, as pointed out above, when the Polyakov loop gets ordered in one of the complex sectors one has no reason to expect localization of the low modes based on “energetic” considerations. This provides a nontrivial test of the standard sea-islands picture: indeed, finding localized low modes in this case would require one to reconsider or at least refine it.

Quite surprisingly, while there is little doubt about its existence, the deconfinement transition in \mathbb{Z}_3 gauge theory in 2+1 dimensions has not been previously studied in detail. While there are extensive studies in the literature concerning \mathbb{Z}_2 [36] and $\mathbb{Z}_{N \geq 5}$ [37–40], no determination of the critical temperature has been done for \mathbb{Z}_3 . As a preliminary task we then need to determine the deconfinement temperature. This is most efficiently done exploiting the duality with the 3-color Potts model (see, e.g., Ref. [41]), which allows one to employ a straightforward cluster algorithm [42, 43] for the numerical simulations. (Incidentally, the critical temperature for the \mathbb{Z}_4 model is straightforwardly obtained by exploiting its equivalence with the $\mathbb{Z}_2 \times \mathbb{Z}_2$ model at half of the coupling, and is simply twice that of the \mathbb{Z}_2 model, determined in Ref. [36]. The equivalence of the \mathbb{Z}_4 and $\mathbb{Z}_2 \times \mathbb{Z}_2$ models follows from their being dual respectively to the four-state clock model and to a decoupled pair of Ising models [41], and from the equivalence of these two models [44].)

The plan of the paper is the following. In Section II we briefly review \mathbb{Z}_3 gauge theory in 2+1 dimensions, focussing in particular on its duality with the 3-color Potts model, while in Section III we briefly review localization of Dirac modes and how it can be detected. In Section IV we revisit the standard sea-islands picture and its formulation in the language of the “Dirac-Anderson Hamiltonian” for staggered fermions, and provide a refined pic-

ture that better appreciates the role of the spatial hopping terms. In Section V we report our results on the deconfinement transition of \mathbb{Z}_3 , concerning in particular the critical temperature and the nature of the transition. In Section VI we study the localization properties of staggered Dirac modes, in both phases of this model and, in the deconfined phase, both in the real and in the complex Polyakov-loop sectors, testing in particular the expectations of the standard and of the refined sea-islands pictures. Finally, in Section VII we draw our conclusions and show prospects for the future. A few technical details related to duality and to the sea-islands picture are discussed in Appendices A and B, respectively.

II. \mathbb{Z}_3 LATTICE GAUGE THEORY IN 2+1 DIMENSIONS

The Wilson action $S_{\mathbb{Z}_3}$ for finite-temperature \mathbb{Z}_3 lattice gauge theory in 2+1 dimensions and the corresponding partition function $Z_{\mathbb{Z}_3}$ read

$$\begin{aligned} Z_{\mathbb{Z}_3}(\beta) &= \sum_{\{U_\mu(n)\}} e^{-S_{\mathbb{Z}_3}[U;\beta]}, \\ S_{\mathbb{Z}_3}[U;\beta] &= \beta \sum_n \sum_{\substack{\mu, \nu=1 \\ \mu < \nu}}^3 (1 - \text{Re} U_{\mu\nu}(n)), \end{aligned} \quad (1)$$

where $n = (n_1, n_2, n_3) = (\vec{x}, t)$ runs over the sites of a cubic $\mathcal{V} = N_1 N_2 N_3 = V N_3$ lattice, $n_\mu = 0, \dots, N_\mu - 1$; $\hat{\mu}$ denotes the unit lattice vector in direction μ ; the sum is over all configurations of link variables $U_\mu(n)$ taking values in \mathbb{Z}_3 , $U_\mu(n) = e^{i\frac{2\pi}{3}k_\mu(n)}$, with $k_\mu(n) = 0, 1, 2$; and $U_{\mu\nu}(n)$ are the plaquette variables associated with elementary squares of the lattice,

$$U_{\mu\nu}(n) = U_\mu(n)U_\nu(n+\hat{\mu})U_{-\mu}(n+\hat{\mu}+\hat{\nu})U_{-\nu}(n+\hat{\nu}), \quad (2)$$

where $U_{-\mu}(n) = U_\mu(n - \hat{\mu})^*$. Periodic boundary conditions are imposed in all directions. At finite temperature, the “temporal” extension $N_t = N_3$ is kept fixed while the “spatial” extensions $N_{1,2}$ are eventually sent to infinity, typically setting $N_s = N_1 = N_2$. In terms of the (mass-dimension 1/2) gauge coupling e and of the lattice spacing a , one has $\beta = 1/(e^2 a)$, and so the temperature of the system is $T/e^2 = \beta/N_t$.

A. Duality

For a lattice of infinite size, the partition function of the \mathbb{Z}_3 gauge theory can be recast as that of a 3-state clock (or vector Potts) model (see, e.g., Ref. [41]). This is true also for a lattice of finite size, provided one sums over all choices of cyclically shifted boundary conditions, i.e.,

$$Z_{\mathbb{Z}_3}(\beta) = z(\tilde{\beta}) \sum_{\{B_\mu\}} Z_{\text{clock}}^{\{B_\mu\}}(\tilde{\beta}), \quad (3)$$

where $z(\tilde{\beta})$ is a numerical prefactor, while the partition functions $Z_{\text{clock}}^{\{B_\mu\}}$,

$$\begin{aligned} Z_{\text{clock}}^{\{B_\mu\}}(\tilde{\beta}) &= \sum_{\{s(n)\}} e^{-S_{\text{clock}}^{\{B_\mu\}}[s;\tilde{\beta}]}, \\ S_{\text{clock}}^{\{B_\mu\}}[s;\tilde{\beta}] &= \tilde{\beta} \sum_n \sum_{\mu=1}^3 (1 - \text{Re} s(n)s(n+\hat{\mu})^*), \end{aligned} \quad (4)$$

describe the interaction of complex spin variables $s(n) = e^{i\frac{2\pi}{3}\sigma(n)}$, $\sigma(n) = 0, 1, 2$, with boundary conditions $\{B_\mu\}$,

$$s(n + N_\mu \hat{\mu}) = B_\mu s(n), \quad \mu = 1, 2, 3, \quad (5)$$

where $B_\mu = e^{i\frac{2\pi}{3}b_\mu}$, $b_\mu = 0, 1, 2$. In Eq. (3) the dual coupling $\tilde{\beta}$ is set to

$$e^{\frac{3\tilde{\beta}}{2}} = \frac{1 + 2e^{-\frac{3\beta}{2}}}{1 - e^{-\frac{3\beta}{2}}}. \quad (6)$$

The need to sum over suitable boundary conditions to have an exact duality in a finite volume is well known [36, 45–47]. A simple general argument showing that shifted boundary conditions are needed for \mathbb{Z}_N gauge theory is given in Appendix A. The effect of such boundary conditions has been discussed in Refs. [36, 46, 47]. The presence of nontrivial $B_{1,2}$ in the spatial boundary conditions leads only to finite-size corrections to the free energy with respect to the trivial case. For the temporal boundary conditions, a nontrivial B_3 leads in the ordered phase to the formation of a spacelike interface between differently ordered domains, and so to an increase in the corresponding free energy and a suppression of the corresponding partition function $Z_{\text{clock}}^{\{B_\mu\}}$. In the disordered phase, instead, a nontrivial B_3 leads only to finite-size corrections, and so all $Z_{\text{clock}}^{\{B_\mu\}}$ are equal in the thermodynamic limit. In both phases one can then restrict to $Z_{\text{clock}} \equiv Z_{\text{clock}}^{\{B_\mu=1\}}$ and obtain the correct $V \rightarrow \infty$ limit for thermodynamic observables. It is worth mentioning that the 3-state clock model is equivalent to the 3-color Potts model,

$$\begin{aligned} Z_{\text{clock}}(\tilde{\beta}) &= Z_{\text{Potts}}(\tfrac{3}{2}\tilde{\beta}), \\ Z_{\text{Potts}}(\tilde{\beta}) &= \sum_{\{s(n)\}} e^{-S_{\text{Potts}}[s;\tilde{\beta}]}, \\ S_{\text{Potts}}[s;\tilde{\beta}] &= \tilde{\beta} \sum_n \sum_{\mu=1}^3 (1 - \delta_{\sigma(n), \sigma(n+\hat{\mu})}). \end{aligned} \quad (7)$$

This is actually true irrespectively of the dimension and of the (matching) choice of boundary conditions.

B. Critical behavior

The 2+1 dimensional \mathbb{Z}_3 gauge theory is expected to display a deconfinement transition at some critical $\beta_c =$

$\beta_c(N_t)$, where the local Polyakov loops,

$$P(\vec{x}) \equiv \prod_{t=0}^{N_t-1} U_3(\vec{x}, t), \quad (8)$$

align to one of the center elements $e^{i\frac{2\pi z}{3}}$, $z = 0, 1, 2$ (of course an Abelian group coincides with its center), and the center symmetry of the model under the transformation

$$U_3(\vec{x}, N_t - 1) \rightarrow e^{i\frac{2\pi z}{3}} U_3(\vec{x}, N_t - 1), \quad \forall \vec{x}, \quad (9)$$

breaks down spontaneously. The duality relation discussed above implies that the critical behavior of this model is the same as that of the 3-color Potts model in a thin-film, 2+1 dimensional geometry, which in turn is expected to match that of the corresponding two-dimensional model. We then expect the deconfinement transition in 2+1 dimensional \mathbb{Z}_3 gauge theory to be second order, and in the same universality class as that of the two-dimensional 3-color Potts model, whose critical exponents are known (see, e.g., Ref. [48]).

From the numerical point of view, it is convenient to determine $\beta_c(N_t)$ by exploiting the duality relation and determining instead the critical coupling $\bar{\beta}_c(N_t)$ of the 2+1 dimensional 3-color Potts model, for which one can use a cluster algorithm [42, 43] and overcome the critical slowing down of local update algorithms near the transition. A convenient (complex) order parameter for the Potts model is the quantity

$$\Phi = \frac{1}{V} \sum_n e^{i\frac{2\pi}{3}\sigma(n)}, \quad (10)$$

whose expectation value vanishes in the low- $\bar{\beta}$, disordered phase and is nonzero in the high- $\bar{\beta}$, ordered phase. To determine the critical coupling we performed a finite-size-scaling study of the following Binder parameter [49],

$$\mathcal{B} = \frac{\langle |\Phi|^4 \rangle}{\langle |\Phi|^2 \rangle^2}, \quad (11)$$

where $\langle \dots \rangle$ denotes the expectation value associated with the partition function Z_{Potts} , Eq. (7). In the disordered phase, in the large-volume limit Φ is expected to obey a (two-dimensional) Gaussian distribution centered at the origin, and so $\mathcal{B} \rightarrow 2$ as the system size $L = N_s$ tends to infinity. In the ordered phase, instead, the distribution of Φ is peaked at a non-zero value and $\mathcal{B} \rightarrow 1$ as $L \rightarrow \infty$. Under the usual one-parameter scaling hypothesis, near the critical coupling $\bar{\beta}_c$ one has that \mathcal{B} depends only on the ratio of the (infinite-volume) correlation length $\xi \sim |\bar{\beta} - \bar{\beta}_c|^{-\nu}$ and L , $\mathcal{B} = F(\xi/L)$. Since this must be an analytic function of β as long as L is finite, one finds

$$\mathcal{B}(\bar{\beta}, L) = f\left((\bar{\beta} - \bar{\beta}_c)L^{\frac{1}{\nu}}\right), \quad (12)$$

for some analytic function f , and so at $\bar{\beta}_c$ the Binder parameter is scale invariant.

III. LOCALIZATION OF DIRAC EIGENMODES

In this Section we briefly discuss eigenmode localization and how to detect it. Full accounts can be found in the literature (see, e.g., Refs. [1, 50, 51]). In this paper we investigate the localization properties of the eigenmodes of the staggered Dirac operator,

$$D_{n,n'}^{\text{stag}} = \frac{1}{2} \sum_{\mu=1}^3 \eta_{\mu}(n) (U_{\mu}(n) \delta_{n+\hat{\mu}, n'} - U_{-\mu}(n) \delta_{n-\hat{\mu}, n'}) ,$$

$$\eta_{\mu}(n) = (-1)^{\sum_{\nu < \mu} n_{\nu}}, \quad (13)$$

computed in the background of gauge field configurations obtained in \mathbb{Z}_3 pure gauge theory. Periodic boundary conditions in the spatial directions and antiperiodic boundary conditions in the temporal direction are understood. In this context D^{stag} acts simply as a probe of the gauge dynamics, which does not include any backreaction from the fermionic modes.

In the deconfined phase of the theory, the eigenmodes of D^{stag} should be studied separately for the different center sectors, characterized by the center element closest to the spatially averaged Polyakov loop,

$$\bar{P} \equiv \frac{1}{V} \sum_{\vec{x}} P(\vec{x}). \quad (14)$$

One can in fact imagine including very heavy dynamical staggered fermions, which explicitly break the center symmetry of the theory and favor the trivial center sector, and then remove them by sending their mass to infinity. In this limit center symmetry is not broken explicitly, but it is broken spontaneously in the deconfined phase, with the trivial center sector being selected by the procedure outlined above. The same procedure but in the presence of a suitable imaginary chemical potential selects instead one of the complex sectors. In practice, in the deconfined phase one simply studies the eigenmodes of D^{stag} restricting to configurations in the center sector of interest. The change in the properties of the eigenmodes of D^{stag} as the pure gauge system transitions from the confined phase to the deconfined phase in a specific center sector then reflects how (infinitely) heavy staggered fermions see the phase transition (see Ref. [12] for a more detailed discussion).

Since D^{stag} is anti-Hermitian, its eigenmodes have purely imaginary eigenvalues, $D^{\text{stag}}\psi_l = i\lambda_l\psi_l$, $\lambda_l \in \mathbb{R}$. Moreover, the spectrum $\{\lambda_l\}$ is symmetric about the origin due to the chiral property $\{\eta_5, D^{\text{stag}}\} = 0$, where $\eta_5(n) = (-1)^{\sum_{\nu} n_{\nu}}$, so that $D^{\text{stag}}\eta_5\psi_l = -i\lambda_l\eta_5\psi_l$. Since also the eigenmode amplitude squared, $|\psi_l(n)|^2$, is the same for ψ_l and $\eta_5\psi_l$, it suffices to restrict our attention to $\lambda_l \geq 0$. It is understood that eigenmodes are normalized, $\sum_n |\psi_l(n)|^2 = 1$.

A. Participation ratio

The staggered operator is technically ($-i$ times) the Hamiltonian of a disordered system, with disorder provided by the fluctuations of the gauge links. For gauge theories with a mass gap, disorder (i.e., gauge field) correlations are short-ranged. Such systems are well known in the condensed matter community to display eigenmode localization, typically at the spectrum edge [50, 51]. Whether eigenmodes in a given spectral region are localized or not can be determined quantitatively by studying the volume scaling of their participation ratio (PR),

$$\text{PR}_l \equiv \frac{1}{N_t V} \text{IPR}_l^{-1}, \quad \text{IPR}_l \equiv \sum_n |\psi_l(n)|^4, \quad (15)$$

averaged over configurations and locally in the spectrum. For a generic observable \mathcal{O}_l associated with mode l , we denote this type of average as

$$\overline{\mathcal{O}}(\lambda, V) \equiv \frac{\langle \sum_l \delta(\lambda - \lambda_l) \mathcal{O}_l \rangle}{\mathcal{V} \rho(\lambda)}, \quad (16)$$

where the dependence on the spatial volume is made explicit, $\langle \dots \rangle$ denotes the expectation value associated with the partition function $Z_{\mathbb{Z}_3}$, Eq. (1), and $\rho(\lambda)$ is the spectral density,

$$\rho(\lambda) \equiv \frac{1}{\mathcal{V}} \langle \sum_l \delta(\lambda - \lambda_l) \rangle. \quad (17)$$

The PR effectively measures the fraction of the system occupied by an eigenmode. As $V \rightarrow \infty$, in a spatially two-dimensional system one expects

$$\overline{\text{PR}}(\lambda, V) \sim c(\lambda) V^{\frac{\alpha(\lambda)-2}{2}}, \quad (18)$$

for some $0 \leq \alpha(\lambda) \leq 2$, which is referred to as fractal dimension. If modes in a certain spectral region are localized, i.e., if they typically extend over a finite region whose size does not scale with the lattice size, then $\alpha = 0$ in that region. If instead they keep spreading out as the system size increases, then they are delocalized and $\alpha \neq 0$. In particular, for $\alpha = 2$ the modes spread out at the same speed as the system size increases, and so are fully delocalized throughout the system. In the condensed matter literature, “delocalized” is usually reserved for $\alpha = 2$, while modes with $0 < \alpha < 2$ are called “critical”. Instead of the PR, one can equivalently look at the average “size” of the modes, $N_t V \cdot \overline{\text{PR}}(\lambda, V) = \overline{\text{IPR}}^{-1}(\lambda, V)$. In the large-volume limit this quantity tends to a constant for localized modes, while it diverges for delocalized modes.

B. Localization and spectral statistics

Another way to detect localization is by looking at the statistical properties of the spectrum, which reflect the

localization properties of the eigenmodes [52]. Fluctuations of delocalized modes under changes in the gauge field configuration are strongly correlated, and so the corresponding eigenvalues are expected to obey the appropriate type of Random Matrix Theory (RMT) statistics. On the other hand, localized modes are uncorrelated, as they respond essentially only to variations of the gauge fields where they are localized, and so the corresponding eigenvalues are expected to fluctuate independently and obey Poisson statistics. This is most easily revealed by the unfolded spectrum, defined via the following mapping,

$$\lambda_i \rightarrow x_i = \mathcal{V} \int^{\lambda_i} d\lambda \rho(\lambda), \quad (19)$$

for which universal predictions are available both for Poisson and RMT statistics (see, e.g., Ref. [53]). In particular, the probability distribution of the unfolded level spacings $s_i = x_{i+1} - x_i$ is known analytically. For Poisson statistics this is the exponential distribution,

$$p_{\text{P}}(s) = e^{-s}. \quad (20)$$

For RMT statistics the distribution is known from the solution of the Gaussian ensemble in the various symmetry classes, with the unitary one being relevant in the case at hand, but no closed form is available. A good approximation is provided by the so-called Wigner surmise,

$$p_{\text{WS}}(s) = a_\beta s^\beta e^{-b_\beta s^2}, \quad (21)$$

where $\beta = 2$, $a_2 = \frac{32}{\pi^2}$ and $b_2 = \frac{4}{\pi}$ for the unitary class. A transition from localized to delocalized modes in the spectrum corresponds to a change in the local statistical properties of the eigenvalues, which can be monitored by looking at features of the unfolded level spacing distribution $p_\lambda(s)$ computed locally in the spectrum. A practically convenient choice is the integrated probability distribution,

$$I_{s_0}(\lambda, V) = \int_0^{s_0} ds p_\lambda(s) = \overline{\theta^{s_0}}(\lambda, V), \quad (22)$$

where $\overline{\theta^{s_0}}$ is the average in the sense of Eq. (16) of the observable $\theta_l^{s_0} = \theta(s_0 - s_l)$, with $\theta(s)$ the Heaviside function. Here $s_0 \approx 0.508$ is chosen as the first crossing point of the exponential and the Wigner surmise to maximize the difference between the Poisson and RMT expectations for this quantity, which are respectively $I_{s_0}^{\text{P}} \simeq 0.398$ and $I_{s_0}^{\text{WS}} \simeq 0.117$.

C. Anderson transitions

Regions in the spectrum where modes are localized are separated from regions where they are delocalized by “mobility edges”, λ_c , where the localization length diverges and the system undergoes a phase transition along

the spectrum. The nature of such transitions, known as “Anderson transitions”, depends on the dimensionality and the symmetry class of the system [51]. While in three spatial dimensions the known Anderson transitions are all second order (including in finite-temperature QCD [54]), in two spatial dimensions one finds transitions of Berezinskii–Kosterlitz–Thouless (BKT) type for systems in the orthogonal [55] and unitary classes [9, 56] (except at the integer quantum Hall transition [57, 58]). There are indications that an Anderson transition of BKT type is present also in the spectrum of the staggered operator in lattice \mathbb{Z}_2 pure gauge theory in 2+1 dimensions [12], which belongs to the orthogonal class. In a BKT-type Anderson transition, the localization length diverges exponentially in $(\lambda - \lambda_c)^{-\frac{1}{2}}$ at the mobility edge λ_c , and modes change from localized to critical, i.e., delocalized but with a nontrivial fractal dimension $0 < \alpha < 2$, that keeps changing along the spectrum above λ_c . This peculiar behavior affects that of the spectral statistics: for BKT-type Anderson transitions the spectral region beyond the mobility edge does not obey RMT statistics, displaying instead a continuously varying statistics intermediate between Poisson and RMT, reflecting the critical nature of the eigenmodes (see Refs. [9, 56] and references therein). Since the staggered operator in the background of \mathbb{Z}_3 gauge fields is in the unitary class, if an Anderson transition is present one would then expect to observe the features of a BKT-type transition.

D. Correlations with gauge observables

According to the sea-islands mechanism mentioned in the Introduction, in the deconfined phase of a gauge theory one generally expects the low Dirac modes to localize near local fluctuations of the Polyakov loop away from the ordered value. This can be checked by measuring the correlation $\overline{\mathcal{P}}(\lambda, V)$ between modes and Polyakov loops, where

$$\mathcal{P}_l \equiv \sum_{\vec{x}, t} P(\vec{x}) |\psi_l(\vec{x}, t)|^2, \quad (23)$$

and the average is taken according to Eq. (16). For fully delocalized modes one expects $\overline{\mathcal{P}} \simeq \bar{P} = \frac{1}{V} \sum_{\vec{x}} P(\vec{x})$, while for localized modes, that should be concentrated on islands of fluctuations, a clearly different value should be obtained. Notice that in the confined phase, and in the deconfined phase in the real sector, one expects $\text{Im } \overline{\mathcal{P}} = 0$ due to charge-conjugation invariance.

Another interesting correlation to check is that between modes and nontrivial plaquettes. To this end we looked at the quantities $\overline{\mathcal{U}}$ and $\overline{\mathcal{U}}_*$ obtained via Eq. (16) from the following observables,

$$\mathcal{U}_l \equiv \sum_n A(n) |\psi_l(n)|^2, \quad \mathcal{U}_{*l} \equiv \sum_{A(n) > 0} |\psi_l(n)|^2, \quad (24)$$

where

$$A(n) \equiv \frac{2}{3} \text{Re} \sum_{\substack{\mu, \nu=1 \\ \mu < \nu}}^3 [4 - U_{\mu\nu}(n) - U_{\mu\nu}(n - \hat{\mu}) - U_{\mu\nu}(n - \hat{\nu}) - U_{\mu\nu}(n - \hat{\mu} - \hat{\nu})] \quad (25)$$

equals the number of nontrivial plaquettes touching n . The quantity $\overline{\mathcal{U}}$ then counts the average number of nontrivial plaquettes seen by a mode, and so for delocalized modes one expects $\overline{\mathcal{U}} \simeq 8 \langle 1 - U_{\mu\nu} \rangle$. The quantity $\overline{\mathcal{U}}_*$ instead measures how much of the mode weight is found on the corners of nontrivial plaquettes. Both observables measure, in slightly different ways, how sensitive eigenmodes are to nontrivial plaquettes: $\overline{\mathcal{U}}_*$ shows in general how much eigenmodes are attracted to or repelled from such plaquettes, while $\overline{\mathcal{U}}$ shows how attracted eigenmodes are to regions where nontrivial plaquettes cluster together.

IV. SEA-ISLANDS PICTURE AND THE DIRAC-ANDERSON HAMILTONIAN

A more detailed formulation of the sea-islands picture for staggered fermions is based on the “Dirac-Anderson Hamiltonian” formalism, developed in Ref. [21] for non-Abelian theories. While the adaptation to an Abelian theory is straightforward, we review here the derivation in some detail since we are extending the original analysis while adopting a slightly different point of view. We work in $d+1$ dimensions for generality. A few technical details are reported in Appendix B.

A. Dirac-Anderson Hamiltonian

The Dirac-Anderson Hamiltonian H^{DA} is obtained via a unitary transformation Ω as $\Omega^\dagger D^{\text{stag}} \Omega = i H^{\text{DA}}$, where Ω is the matrix of spatially localized eigenvectors of the temporal part ($\mu = d+1$) of D^{stag} . Eigenmodes are labelled by their location $\vec{y} = (y_1, \dots, y_d)$ and by an index $k = 0, \dots, N_t - 1$, corresponding to the N_t Matsubara frequencies $\omega_k(\vec{x})$ associated with the \vec{x} -dependent temporal boundary condition $\psi(\vec{x}, N_t) = -P(\vec{x})\psi(\vec{x}, 0) = -e^{i\phi(\vec{x})}\psi(\vec{x}, 0)$. These are discussed in detail below. For an Abelian theory with a 1-dimensional internal space one has

$$\Omega_{t\vec{x}, k\vec{y}} = \frac{1}{\sqrt{N_t}} \delta_{\vec{x}, \vec{y}} e^{i\omega_k(\vec{x})t} P(\vec{x}, t)^*, \quad (26)$$

where $P(\vec{x}, t+1) = P(\vec{x}, t)U_{d+1}(\vec{x}, t)$, with $P(\vec{x}, 0) = 1$ and $P(\vec{x}, N_t) = P(\vec{x}) = e^{i\phi(\vec{x})}$. The corresponding Dirac-

Anderson Hamiltonian reads

$$H_{k\vec{x},l\vec{y}}^{\text{DA}} = e_k(\vec{x})\delta_{kl}\delta_{\vec{x},\vec{y}} + \frac{1}{2i} \sum_{j=1}^d \eta_j(\vec{x}) [V_{+j}(\vec{x})_{kl}(T_j)_{\vec{x},\vec{y}} - V_{-j}(\vec{x})_{kl}(T_j^\dagger)_{\vec{x},\vec{y}}], \quad (27)$$

with “unperturbed eigenvalues”

$$e_k(\vec{x}) = \eta_{d+1}(\vec{x}) \sin \omega_k(\vec{x}), \quad (28)$$

and hopping terms

$$V_{\pm j}(\vec{x})_{kl} = \frac{1}{N_t} \sum_{t=0}^{N_t-1} e^{-i[\omega_k(\vec{x}) - \omega_l(\vec{x} \pm \hat{j})]t} U_{\pm j}^{\text{tg}}(\vec{x}, t), \quad (29)$$

$$U_{\pm j}^{\text{tg}}(\vec{x}, t) = P(\vec{x}, t) U_{\pm j}(\vec{x}, t) P(\vec{x} \pm \hat{j}, t)^*,$$

where T_j are the spatial translation operators, $(T_j)_{\vec{x},\vec{y}} = \delta_{\vec{x}+\hat{j},\vec{y}}$ (including periodic boundary conditions). Here the superscript “tg” denotes links computed in temporal gauge, $U_{d+1}^{\text{tg}}(\vec{x}, t) = 1$, $\forall \vec{x}$, $0 \leq t < N_t - 1$, and we made explicit the fact that η_μ depend only on the spatial coordinates. One has $V_{-j}(\vec{x})_{kl} = V_{+j}(\vec{x} - \hat{j})_{lk}^*$, and one can easily show that $V_{\pm j}(\vec{x})$ are unitary $N_t \times N_t$ matrices.

The Hamiltonian H^{DA} is identical to that of a set of N_t Anderson-like models, with correlated random local potentials $e_k(\vec{x})$, and coupled by the random hopping matrices $V_j(\vec{x})$. At this stage, however, the labelling of the $e_k(\vec{x})$ is arbitrary, and depends on the ordering in k of the basis vectors and on the convention chosen for the Polyakov-loop phase $\phi(\vec{x})$, both of which can as well be \vec{x} -dependent. This is formally expressed by writing

$$\omega_k(\vec{x}) = \tilde{\omega}_{N_k(\vec{x})}(\phi(\vec{x})), \quad \tilde{\omega}_n(\phi) = \frac{\phi + (2n+1)\pi}{N_t}, \quad (30)$$

where $N_k(\vec{x}) = 0, \dots, N_t - 1$ and the convention for the Polyakov-loop phase have to be specified. Without any loss of generality, we can restrict the latter to $\phi(\vec{x}) \in [-\pi, \pi)$ at each site. Notice that since $\sin \tilde{\omega}_{n+\frac{N_t}{2} \bmod N_t} = -\sin \tilde{\omega}_n$, at each \vec{x} half of the $e_k(\vec{x})$ in Eq. (28) are positive and half are negative. A further simplifying choice is then to pair opposite unperturbed eigenvalues so that

$$e_{k+\frac{N_t}{2} \bmod N_t}(\vec{x}) = -e_k(\vec{x}). \quad (31)$$

One can show that in this case

$$V_{\pm j}(\vec{x})_{k+\frac{N_t}{2} \bmod N_t, l+\frac{N_t}{2} \bmod N_t} = V_{\pm j}(\vec{x})_{kl}. \quad (32)$$

The resulting general structure of the Dirac-Anderson Hamiltonian is then

$$H^{\text{DA}} = \begin{pmatrix} E & \mathbf{0} \\ \mathbf{0} & -E \end{pmatrix} + \frac{1}{2i} \sum_{j=1}^d \eta_j \left[\begin{pmatrix} A_j & B_j \\ B_j & A_j \end{pmatrix} T_j - T_j^\dagger \begin{pmatrix} A_j^\dagger & B_j^\dagger \\ B_j^\dagger & A_j^\dagger \end{pmatrix} \right], \quad (33)$$

where $E(\vec{x})$, $A_j(\vec{x})$, $B_j(\vec{x})$ are $\frac{N_t}{2} \times \frac{N_t}{2}$ matrices, with E diagonal, $A_j^\dagger A_j + B_j^\dagger B_j = \mathbf{1}$ and $A_j^\dagger B_j + B_j^\dagger A_j = \mathbf{0}$. Here $\mathbf{0}$ and $\mathbf{1}$ are the $\frac{N_t}{2}$ -dimensional zero and identity matrices, respectively.

The simplest possibility for $N_k(\vec{x})$ is clearly $N_k^{(0)}(\vec{x}) = k$, which with our convention on $\phi(\vec{x})$ satisfies the above requirements. This was used in Ref. [21]. However, the ordering of the $e_k(\vec{x})$ obtained with this choice generally does not reflect their rank in magnitude. To give the $e_k(\vec{x})$ an interpretation as the different “energy levels” of an electron in the potential of an atom sitting at the spatial lattice site \vec{x} , it is convenient to order the basis vectors so that $e_k(\vec{x})$ are positive for $0 \leq k \leq \frac{N_t}{2} - 1$ and negative for $\frac{N_t}{2} \leq k \leq N_t - 1$, and in both cases ranked by absolute value, i.e.,

$$0 \leq e_0(\vec{x}) \leq e_1(\vec{x}) \leq \dots \leq e_{\frac{N_t}{2}-1}(\vec{x}), \quad (34)$$

with $e_{\frac{N_t}{2}+k}(\vec{x}) = -e_k(\vec{x})$, $k = 0, \dots, \frac{N_t}{2} - 1$. The diagonal matrix E in Eq. (33) in this case is then positive-semidefinite. This implicitly defines $N_k(\vec{x})$ so that a given k always corresponds to the energy level of the same rank at each spatial site, thus giving k an intrinsic meaning. An explicit expression for $N_k(\vec{x})$ can be worked out analytically, and is reported in Appendix B 1. In particular, the lowest positive energy level at each site depends only on $\phi(\vec{x})$ and reads

$$e_0(\vec{x}) = \mathcal{E}(\phi(\vec{x})) = \sin \frac{\pi - |\phi(\vec{x})|}{N_t}. \quad (35)$$

Moreover, $e_k(\vec{x})$ remains unchanged under the replacement $\phi(\vec{x}) \rightarrow -\phi(\vec{x})$.

Irrespectively of the choice of $N_k(\vec{x})$, the Dirac-Anderson form of the staggered operator leads one to expect, by analogy with the usual Anderson models, that modes at the high end of the spectrum are localized, independently of the phase of the gauge system. Since the ordering of the Polyakov loop at the deconfinement transition is expected to open a pseudogap in the spectrum near the origin, thus making the near-zero region qualitatively similar to a spectrum edge, one can understand also localization of the low modes in the deconfined phase by analogy with the usual Anderson models. However, this intuitive explanation should be supplemented by a more detailed mechanism if one wants to understand better the connection between low-mode localization and deconfinement.

B. Standard sea-islands picture

As a first step in this direction, the formalism of the Dirac-Anderson Hamiltonian discussed above allows one to formulate the sea-islands picture more precisely. In fact, the twist on the fermion wave functions provided by the effective local temporal boundary conditions $\psi(\vec{x}, N_t) = -P(\vec{x})\psi(\vec{x}, 0)$ can be quantified by the

lowest energy level $\mathcal{E}(\phi(\vec{x}))$, Eq. (35). The sea-islands picture then amounts to state that places with lower \mathcal{E} are “energetically” favorable for the localization of Dirac eigenmodes. This can be tested in detail by looking at how much weight is allocated on the different “branches” of the wave function corresponding to the different energy levels, and how this correlates with the energy levels themselves.

The components $\Psi_l(\vec{x}, k)$ of the l th eigenvector in the new basis are obtained from $\Psi_l = \Omega \psi_l$, and read

$$\Psi_l(\vec{x}, k) = \frac{1}{\sqrt{N_t}} \sum_{t=0}^{N_t-1} e^{-i\omega_k(\vec{x})t} P(\vec{x}, t) \psi_l(\vec{x}, t). \quad (36)$$

Clearly, $H^{\text{DA}} \Psi_l = \lambda_l \Psi_l$. For each mode, the weight on branch k is

$$w_l(k) = \sum_{\vec{x}} |\Psi_l(\vec{x}, k)|^2, \quad (37)$$

and the corresponding unperturbed energy averaged over spatial sites is

$$\varepsilon_l(k) = \frac{1}{w_l(k)} \sum_{\vec{x}} e_k(\vec{x}) |\Psi_l(\vec{x}, k)|^2. \quad (38)$$

It is easy to show that the components $\Psi_{-l}(\vec{x}, k)$ of $\eta_5 \psi_l$ (corresponding to eigenvalue $-\lambda_l$) in the new basis are

$$\Psi_{-l}(\vec{x}, k) = \eta_{d+1}(\vec{x}) \Psi_l(\vec{x}, k + \frac{N_t}{2} \bmod N_t), \quad (39)$$

and so for the corresponding weights one finds $w_{-l}(k) = w_l(k + \frac{N_t}{2} \bmod N_t)$.

The sea-islands picture leads one to expect, perhaps naïvely, that low positive (resp. negative) modes, if present, have a large weight $w_l(0)$ (resp. $w_l(\frac{N_t}{2})$), and correspondingly $\varepsilon_l(0)$ should be close to the most favorable value of \mathcal{E} (resp. its negative), leading to localization when such favorable places are rare.

C. Refined sea-islands picture

While the idea of interpreting sites with low $\mathcal{E}(\phi(\vec{x}))$ as “energetically” favorable for the eigenmodes is suggestive, the fact that H^{DA} is not positive-definite makes it questionable. On the other hand, the correlation between such sites and the localization centers of low localized modes is evident in the numerical data [7, 12, 18, 19]. We now argue that this correlation can be better explained in an indirect way, which will lead us to a refinement of the sea-islands mechanism.

In the high-temperature phase one expects the ordering of the Polyakov loops to induce strong correlations among time slices. One then expects to a first approximation that $P(\vec{x}) \approx P_* = e^{i\phi_*}$ and $U_j^{\text{tg}}(\vec{x}, t) \approx U_{j*}^{\text{tg}}(\vec{x})$, and so E to be approximately \vec{x} -independent. An explicit calculation [see Appendix B 2, Eq. (B4)] shows that in this case $V_j(\vec{x})_{kl} \approx \delta_{k, l + \frac{N_t}{2} \bmod N_t} U_{j*}^{\text{tg}}(\vec{x})$, or in other words

$A_j(\vec{x}) \approx \mathbf{0}$ and $B_j(\vec{x}) \approx U_{j*}^{\text{tg}}(\vec{x}) \mathbf{1}$. Notice that this does not depend on the detailed definition of $N_k(\vec{x})$ as long as Eq. (31) is enforced and the sign of $e_k(\vec{x})$ at fixed k is constant throughout the lattice: The actual ordering of the positive unperturbed eigenvalues is then immaterial, as it should be. In this case

$$(H^{\text{DA}})^2 \approx E^2 + \left[\frac{1}{2i} \sum_{j=1}^d \eta_j (B_j T_j - T_j^\dagger B_j^\dagger) \right]^2 \equiv H_B^2, \quad (40)$$

and so generally a gap of size $[\mathcal{E}(\phi_*)]^2$ opens in the spectrum of $(H^{\text{DA}})^2$. In the opposite limit of $B_j \approx \mathbf{0}$ and A_j approximately proportional to $\mathbf{1}$, again assuming constant E , one finds instead

$$(H^{\text{DA}})^2 \approx \text{diag}(H_+^2, H_-^2) \equiv H_A^2, \quad (41)$$

$$H_\pm = E \pm \frac{1}{2i} \sum_{j=1}^d \eta_j (A_j T_j - T_j^\dagger A_j^\dagger),$$

which generally has an ungapped spectrum. One then generally expects that low modes prefer locations where A_j deviates from zero, and even more so in the deconfined phase, where a large eigenmode amplitude in these regions is required for the corresponding eigenvalue to get below the gap. Since deviations from $B_j^\dagger B_j = \mathbf{1}$ are expected to show up in places where the Polyakov loop is disordered, and since in the deconfined phase these places are rare and spatially well separated from each other, this makes them able to localize the low eigenmodes. While $A_j \approx \mathbf{1}$ is unlikely to happen since it requires strong anticorrelation among spatial links across different time-slices [see Appendix B 2, Eq. (B5)], for Hamiltonians intermediate between Eq. (40) and Eq. (41) – H_{AB} -type Hamiltonians, for want of a better name – one still expects a sizeable density of low modes.

To see this in detail, one can switch off the hopping terms connecting the extended B -type region where $A_j \approx \mathbf{0}$ for all j , from AB -type regions where it is non-negligible for some j , and diagonalize separately the Hamiltonians of the resulting independent subsystems. For the first region one finds a Hamiltonian of type H_B , Eq. (40), and so delocalized modes and an almost sharply gapped spectrum. For the second region one finds instead a Hamiltonian of type H_{AB} (or more precisely a set of spatially separated Hamiltonians of this type), intermediate between Eq. (40) and Eq. (41), and so localized modes and an ungapped spectrum, with a small but still sizeable density of low modes. When switching on again the hopping terms at the boundary of the two regions, one finds that the lowest AB -type modes, far below the gap, can hardly mix with the B -type modes due to the large energy difference, and with other AB -type modes due to the large spatial separation, so that they remain localized also when accounting for the full interaction. This argument leads then to a different type of sea-islands picture, where the sea and the islands are defined in terms of the spatial hopping terms, rather than the local potential.

The argument above clarifies the important role played by the ordering of the Polyakov loop and the associated depletion of the near-zero spectral region for the localization of the low modes in the deconfined phase. By contrast, in the confined phase no extended B -type region appears with its almost gapped spectrum, and there seems to be no mechanism preventing delocalization of the low modes, which are likely to display also a larger spectral density.

Notice also that for the same constant matrix E , the spectrum of the Hamiltonian Eq. (41) typically extends to higher values than that of the Hamiltonian Eq. (40). An argument similar to the one above suggests that places where A_j deviates from zero are favorable also for the localization of the high modes in the deconfined phase, with delocalization being prevented by energy or spatial separation. In the confined phase where favorable islands are more frequent, repeating the argument by separating now the regions where A_j is the largest from the rest, one sees that modes localized on the most favorable islands are likely to reach larger eigenvalues, and to remain stable against delocalization when the remaining hopping terms are switched on due to a large energy separation.

The refined sea-islands picture described above provides a more detailed understanding of the microscopic mechanism behind the localization of the low Dirac modes in the deconfined phase of a gauge theory. On the one hand, it does not contradict but rather subsume the standard sea-islands picture in the physical, real Polyakov-loop sector, since local disorder leading to $A_j \neq 0$ is naturally associated with Polyakov-loop fluctuations, and these automatically lead to a smaller \mathcal{E} . On the other hand, it extends the old picture to cases where there really are no “energetically favorable” islands, such as the deconfined phase of \mathbb{Z}_3 gauge theory in a complex center sector: even in this case the local Polyakov-loop fluctuations are expected to lead to favorable fluctuations in the hopping terms, despite the fact that \mathcal{E} is not lower than in the sea of ordered Polyakov loops. Moreover, fluctuations in the hopping terms could also appear independently of the Polyakov-loop ones: according to the refined picture these would be favorable for localization, while they are overlooked by the standard picture. This is a distinguishing signature that can be looked for in numerical data.

As a final remark, we note that the argument above can be easily extended to non-Abelian theories after dealing with only minor technical complications: this is discussed in Appendix B3.

V. DECONFINEMENT TRANSITION

In this Section we report our numerical results on the deconfinement transition in 2+1 dimensional \mathbb{Z}_3 gauge theory, determined via duality from a study of the corresponding 3-color Potts model. Periodic boundary con-

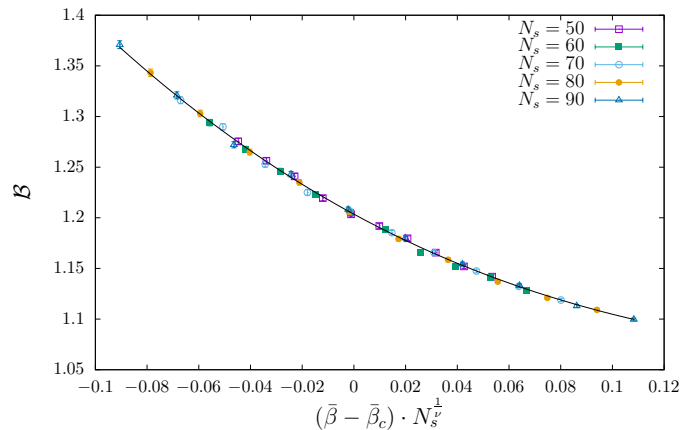


FIG. 1. The Binder parameter \mathcal{B} , Eq. (11), for the 2+1 dimensional 3-color Potts model as a function of the coupling, for temporal size $N_t = 4$ and various spatial sizes N_s . The solid line shows the result of a fit to the data with Eq. (42), for $n = 6$.

N_t	N_s	configurations	fitting range
2	50,60,70,80,90	20000	[0.6372,0.6381]
4	50,60,70,80,90	20000	[0.5640,0.5649]
6	90,100,110,120,130	20000	[0.5546,0.5557]

TABLE I. Simulation and analysis details for the study of the 2+1 dimensional 3-color Potts model for temporal extension N_t .

ditions are understood on both sides of the duality (see the discussion in Section II A).

After a preliminary sweep with a standard Metropolis algorithm to bracket the transition, we performed numerical simulations with a standard cluster algorithm [42, 43] near the critical coupling of the 2+1 dimensional 3-color Potts model on a cubic $N_s^2 \times N_t$ lattice. Keeping the temporal extension fixed to $N_t = 2, 4, 6$, we determined the critical coupling $\bar{\beta}_c(N_t)$ by means of a finite-size-scaling analysis of the Binder parameter \mathcal{B} , Eq. (11). We measured \mathcal{B} on a sample of well decorrelated configurations, estimating its statistical error by a standard jackknife procedure. For the finite-size-scaling analysis we made the usual one-parameter scaling hypothesis, leading to Eq. (12), which we subsequently approximated by a polynomial of order n ,

$$\mathcal{B}(\bar{\beta}, N_s) = \sum_{j=0}^n f_j u(\bar{\beta}, N_s)^j, \quad (42)$$

$$u(\bar{\beta}, N_s) = (\bar{\beta} - \bar{\beta}_c) N_s^{\frac{1}{\nu}}.$$

We then fitted our numerical data with Eq. (42) using the constrained fitting approach of Ref. [59], varying the order n of the polynomial until the errors on the fitting parameters stabilize. Through this procedure, the error estimate from the fitting routine already takes into account the systematic effect due to the truncation of

N_t	$\bar{\beta}_c$	ν	\mathcal{B}_c	β_c
2	0.637700(15)	0.772(63)	1.1737(13)	0.982070(16)
4	0.5644100(73)	0.846(30)	1.2036(17)	1.0670181(90)
6	0.555176(56)	0.799(36)	1.2246(28)	1.078506(70)

TABLE II. Critical coupling $\bar{\beta}_c$, correlation length critical exponent ν and critical Binder parameter \mathcal{B}_c of the 2+1 dimensional 3-color Potts model for temporal extension N_t , and corresponding critical coupling β_c of 2+1 dimensional \mathbb{Z}_3 gauge theory.

Eq. (42). Fits were performed using the MINUIT library [60, 61]. We did not use any priors for $\bar{\beta}_c$ and ν , and very broad Gaussian priors for the coefficients f_n . Errors turn out to be stable already at $n = 6$. Details on the volumes, statistics, and fitting ranges employed in the analysis are reported in Tab. I. Our results for the critical coupling $\bar{\beta}_c$, the correlation length critical exponent ν , and the critical Binder parameter $\mathcal{B}_c = f_0$ are reported in Tab. II. There we also report the dual critical coupling β_c , at which the deconfinement transition takes place in \mathbb{Z}_3 gauge theory. The quality of the resulting collapse plot shown in Fig. 1 confirms the goodness of the one-parameter scaling assumption. The critical exponent ν is in good agreement with the value $\nu^{2d \text{ Potts}} = \frac{5}{6}$ of the 2-dimensional 3-color Potts models [48], confirming the second-order nature and universality class of the transition expected from universality arguments (see Section II B). For comparison, the critical parameters of the two-dimensional model are $\beta_c^{2d \text{ Potts}} = \log(1 + \sqrt{3})$ [48, 62] and $\mathcal{B}_c^{2d \text{ Potts}} = 1.16(1)$ [63].

VI. LOCALIZATION OF STAGGERED MODES: NUMERICAL RESULTS

We numerically simulated pure \mathbb{Z}_3 gauge theory on 2+1 dimensional $N_s^2 \times N_t$ lattices, with $N_t = 4$ and $N_s = 20, 24, 28, 32$, and with β values on both sides of the deconfinement transition, using a standard Metropolis algorithm. For each β and N_s we collected 1500 well decorrelated gauge configurations, and for each of them we computed the full set of eigenvalues and eigenvectors of the staggered Dirac operator, Eq. (13), using the LAPACK library [64]. We also measured the local plaquettes and Polyakov loops in order to study their correlation with the staggered eigenmodes.

As explained in Section III, in the deconfined phase ($\beta > \beta_c$) averages are computed separately for configurations in the physical, real Polyakov-loop sector ($\text{Im } \bar{P} = 0$, $\text{Re } \bar{P} > 0$) and in the complex sectors ($\text{Im } \bar{P} \neq 0$, $\text{Re } \bar{P} < 0$). Since the two complex sectors $\text{Im } \bar{P} \gtrless 0$ yield identical results thanks to C -invariance, it suffices to study the sector $\text{Im } \bar{P} > 0$. To ensure that configurations are in the desired center sector we make a suitable center transformation, Eq. (9), whenever needed, thus

effectively collecting 1500 configurations in both sectors under study. In the confined phase ($\beta < \beta_c$) where center symmetry is realized, averages are instead computed over the full set of configurations, covering evenly all the sectors.

For a finite ensemble of gauge configurations, the local averages $\overline{\mathcal{O}}(\lambda, V)$, Eq. (16), are estimated by averaging over the modes in small disjoint intervals of equal width $\Delta\lambda = 0.05$ (in lattice units), and assigning the result to the average eigenvalue in the bin. Errors are estimated via the standard jackknife method. Additional care is required for the calculation of the PR in the presence of degenerate eigenvalues, which do show up in discrete gauge theories in small and moderate volumes (see Ref. [12] for the case of \mathbb{Z}_2). In this case a single value of the PR is assigned to the whole degenerate subspace by means of a suitable average, and included in the bin average with multiplicity equal to the dimension of the subspace (see the appendix of Ref. [12] for details). The fractal dimension is then estimated from $\overline{\text{PR}}(\lambda, V)$ using pairs of system spatial sizes $N_{s1,2}$ via

$$\alpha(\lambda; N_{s1}, N_{s2}) = 2 + \frac{\log[\overline{\text{PR}}(\lambda, N_{s1}^2)/\overline{\text{PR}}(\lambda, N_{s2}^2)]}{\log(N_{s1}/N_{s2})}. \quad (43)$$

The corresponding error is obtained by standard linear propagation. For sufficiently large volumes where eigenvalues become dense, unfolded spacings can be computed by dividing the level spacings $\lambda_{i+1} - \lambda_i$ by the average level spacing $(\mathcal{V}\rho)^{-1}$, i.e.,

$$\begin{aligned} s_i &= x_{i+1} - x_i = \mathcal{V} \int_{\lambda_i}^{\lambda_{i+1}} d\lambda \rho(\lambda) \\ &\simeq (\lambda_{i+1} - \lambda_i) \mathcal{V}\rho(\lambda_i). \end{aligned} \quad (44)$$

For a finite ensemble, this is done in practice by estimating the average spacing in each spectral bin by including those spacings $\lambda_{l+1} - \lambda_l$ for which λ_l lies in the bin, and dividing $\lambda_{i+1} - \lambda_i$ by the average spacing in the bin where λ_i belongs. Other definitions are possible (e.g., one could include in each bin average only those spacings for which the middle point between the eigenvalues lies in the bin), but they are all equivalent in the large-volume limit. This practical definition of unfolded spacings avoids problems with accidental degeneracies of eigenvalues.

In the deconfined phase the Polyakov loops become spatially ordered, breaking spontaneously the center symmetry of the system, and inducing strong correlations among different time slices. In a first approximation, typical gauge configurations can be thought of as fluctuating around the perfectly ordered configuration $P(\vec{x}) = e^{i\phi_0}$ with spatial links all equal to unity. A fermion in this gauge background is equivalent to a free fermion subject to nontrivial temporal boundary conditions, a setup for which the staggered operator can be diagonalized exactly. The positive eigenvalues read

$$\lambda_{k,j_1,j_2} = \sqrt{(\sin \omega_k)^2 + (\sin p_{j_1})^2 + (\sin p_{j_2})^2}, \quad (45)$$

where $\omega_k = \frac{\phi_0 + (2k+1)\pi}{N_t}$ with $k = 0, \dots, N_t - 1$, and $p_{j_{1,2}} = \frac{2\pi j_{1,2}}{N_s}$ with $j_{1,2} = 0, \dots, N_s - 1$. The free spectrum Eq. (45) lies in the interval $[\lambda_L, \lambda_H]$ where

$$\lambda_L = \min_k |\sin \omega_k|, \quad \lambda_H = \sqrt{\max_k (\sin \omega_k)^2 + 2}. \quad (46)$$

When looking at the results for the interacting spectrum in the deconfined phase, one can use the endpoints of the free spectrum for the appropriate values of ϕ_0 and N_t to separate the bulk from the low modes ($\lambda < \lambda_L$) and the high modes ($\lambda > \lambda_H$). These points are marked by vertical dashed lines in our figures. For $N_t = 4$, in the real sector ($\phi_0 = 0$) one has $\lambda_L^{(r)} = \frac{1}{\sqrt{2}}$ and $\lambda_H^{(r)} = \sqrt{\frac{5}{2}}$, while in the complex sectors ($\phi_0 = \pm \frac{2\pi}{3}$) one has $\lambda_L^{(c)} = \sin \frac{\pi}{12}$ and $\lambda_H^{(c)} = \sqrt{(\sin \frac{5\pi}{12})^2 + 2}$. Since in the confined phase all center sectors contribute, in the corresponding figures all the special points mentioned above are marked by vertical dashed lines. The square root of the average eigenvalue squared, $\lambda_* = \sqrt{\frac{3}{2}}$, is also marked by a solid vertical line in our figures. This point in the spectrum is characterized by a sizeable degeneracy of eigenmodes for the medium-size lattices used here, and often corresponds to a noticeable dip or peak in the plots of the various observables.

A. Mode size, fractal dimension, and spectral statistics

As explained in Section III, localization is conveniently detected by studying the size and the fractal dimension of the eigenmodes, and the statistical properties of the corresponding eigenvalues. Numerical results for the average mode size $N_t V \cdot \overline{\text{PR}}(\lambda, V) = \overline{\text{IPR}}^{-1}(\lambda, V) \sim V^{\alpha(\lambda)}$ and the corresponding fractal dimension $\alpha(\lambda)$, Eq. (18), and for the local average of the integrated unfolded level spacing distribution $I_{s_0}(\lambda, V)$, Eq. (22), are shown in Figs. 2–4 for typical β values both below and above $\beta_c(N_t = 4)$ (see Tab. II), and for different lattice sizes.

1. Confined phase

Results for the confined phase are shown in Fig. 2. In this phase the low modes are delocalized, but with a non-trivial fractal dimension close to 1. A similar behavior was found for gauge group \mathbb{Z}_2 [12]. In the standard language of disordered systems, these modes are therefore critical. As λ increases, modes become more and more delocalized, with an increasing fractal dimension which gets close to 2 as one enters the bulk of the spectrum. Our estimates of α remain always slightly smaller than 2, but this may as well be only a finite size effect, with full delocalization eventually reached in the middle of the spectrum for larger volumes. Finally, at the high end of

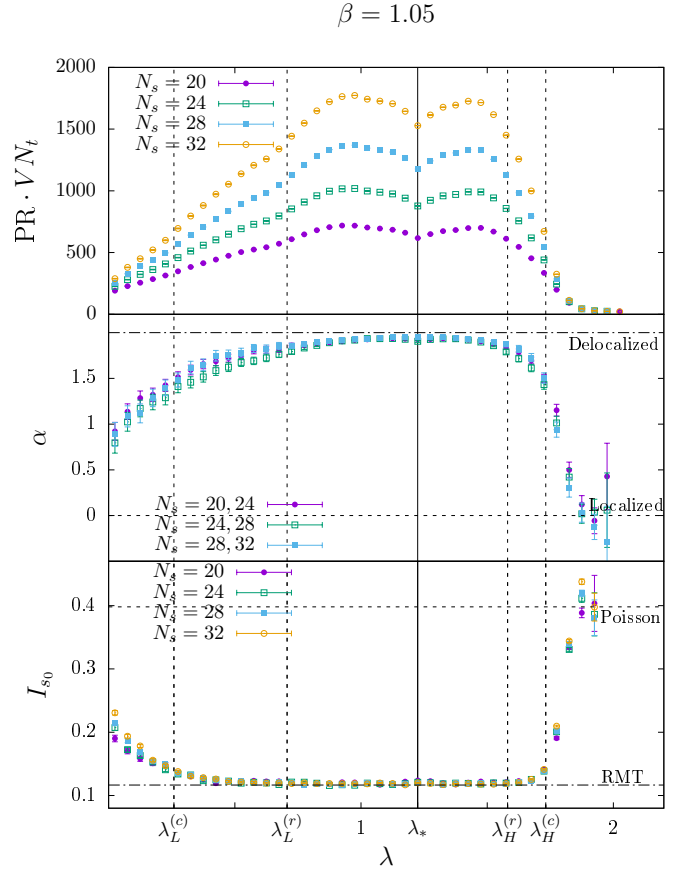


FIG. 2. Eigenmode properties in the confined phase. Top: Mode size. Center: Fractal dimension. Horizontal lines mark expectations for localized (dashed) and fully delocalized modes (dot-dashed). Bottom: Integrated unfolded level spacing distribution. Horizontal lines mark expectations for Poisson (dashed) and RMT statistics (dot-dashed). Here $N_t = 4$.

the spectrum the fractal dimension is compatible with zero, indicating that modes are localized.

Results for I_{s_0} (Fig. 2, bottom) support this picture, with low modes displaying a nontrivial, λ -dependent statistics intermediate between Poisson and RMT, and only mildly dependent on the volume; bulk modes compatible with RMT behavior, except towards both ends of the bulk where they depart from it; and high modes quickly becoming compatible with Poisson statistics. We then expect an extend region of critical modes at the low end of the spectrum, either extending all the way across the bulk or containing a region of fully extended modes; and a region of localised modes at the high end of the spectrum. Which of these alternatives is realized for the bulk modes cannot be decided with the current lattice and gauge ensemble sizes.

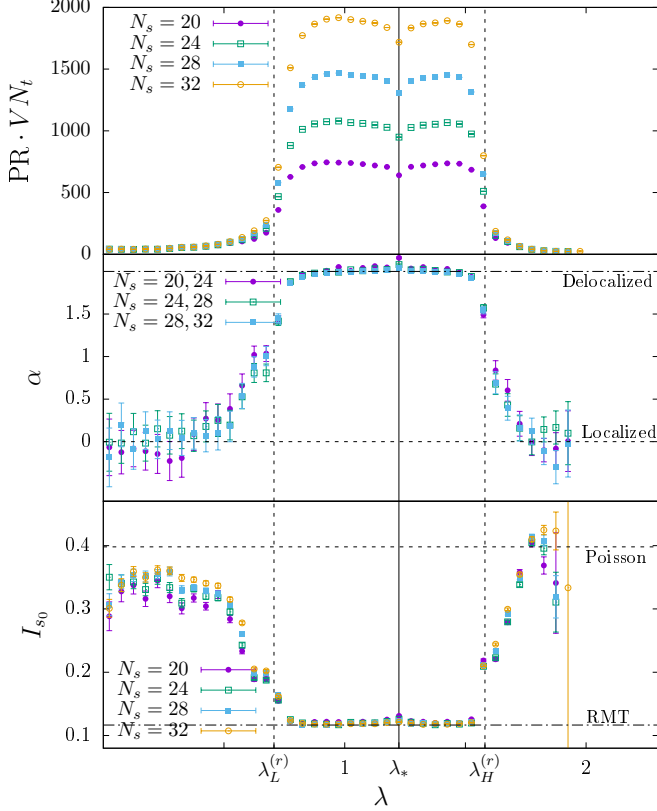
$\beta = 1.08$, Real sector

FIG. 3. Eigenmode properties in the deconfined phase – real sector. Top: Mode size. Center: Fractal dimension. Horizontal lines mark expectations for localized (dashed) and fully delocalized modes (dot-dashed). Bottom: Integrated unfolded level spacing distribution. Horizontal lines mark expectations for Poisson (dashed) and RMT statistics (dot-dashed). Here $N_t = 4$.

2. Deconfined phase

a. Real sector Results for the real sector in the deconfined phase are shown in Fig. 3. There both low and high modes are clearly localized. Bulk modes instead are delocalized, with a fractal dimension quickly rising from around 1 to 2 (i.e., full delocalization) as one enters the bulk from either end. In the transition regions α has little to no volume dependence while being clearly separated from 2. This is the kind of behavior expected for a BKT-type Anderson transition (see Section III C). While difficult to determine precisely with the available data, the mobility edges are found in the vicinity of $\lambda_L^{(r)}$ and $\lambda_H^{(r)}$.

Results for the spectral statistics (Fig. 3, bottom) support the picture obtained from the mode size. In the low-mode region I_{s_0} is rather flat near zero, and closer to the value expected for Poisson statistics than that expected for RMT statistics. More importantly, it shows a tendency to become flatter and closer to the Poisson

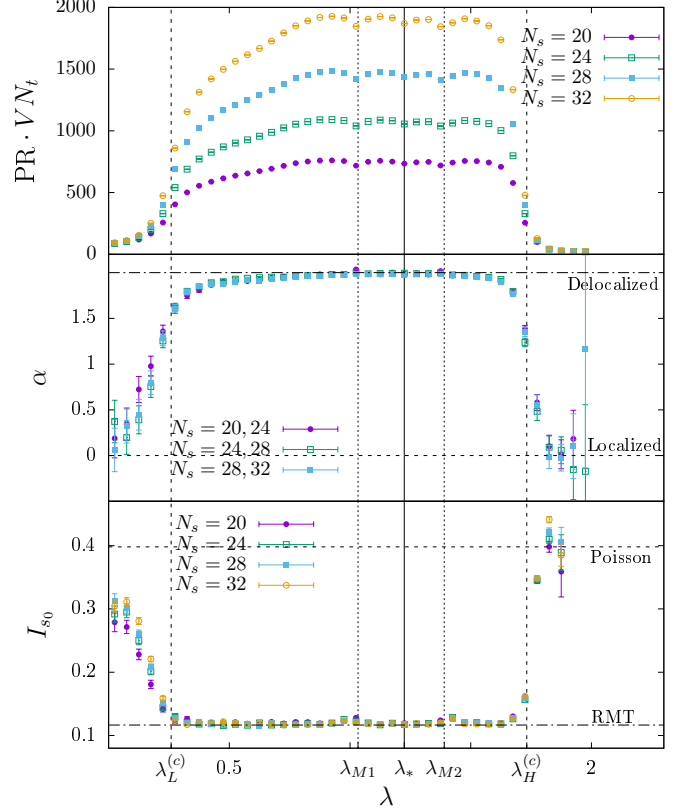
 $\beta = 1.08$, Complex sector

FIG. 4. Eigenmode properties in the deconfined phase – complex sectors. Top: Mode size. Center: Fractal dimension. Horizontal lines mark expectations for localized (dashed) and fully delocalized modes (dot-dashed). Bottom: Integrated unfolded level spacing distribution. Horizontal lines mark expectations for Poisson (dashed) and RMT statistics (dot-dashed). Here $N_t = 4$.

expectation as the volume is increased. Although the volume dependence is not much stronger than in the confined phase, the relative flatness of I_{s_0} at the low end of the spectrum in the deconfined phase suggests that low modes all share the same spectral statistics, as opposed to the changing statistics observed in the confined phase. For bulk and high modes one finds spectral statistics very close respectively to RMT and to Poisson statistics, exactly as in the confined phase. Near the mobility edges one finds for I_{s_0} a value intermediate between the Poisson and the RMT expectation, and approximately volume independent, again supporting the expectation that the Anderson transitions are of BKT type.

b. Complex sectors Results for the complex sectors are shown in Fig. 4. Also in these sectors the low modes appear to be localized, with their fractal dimension (Fig. 4, center) tending to zero as the lattice sizes used for its estimate are increased. As discussed in Sections I and IV C, this cannot be explained in terms of “energetically” favorable islands of Polyakov-loop fluctuations alone. Notice that the mode size of the low modes

is larger in the complex sectors than in the real sector. For bulk and high modes the situation is the same found in the real sector, i.e., bulk modes are delocalized (and fully so deep in the bulk) and high modes are localized, with mobility edges again in the vicinity of $\lambda_L^{(c)}$ and $\lambda_H^{(c)}$, therefore different from those found in the real sector and closer to the spectrum edges.

In Fig. 4, and in all other plots concerning the complex sectors in the deconfined phase, we also show two other special points in the spectrum, λ_{M1} and λ_{M2} , marked by vertical dotted lines. These correspond to choosing $j_{1,2}$ so that $(\sin p_{j_1})^2 + (\sin p_{j_2})^2 = 1$, and $k = 0$ or 1 , corresponding to $\sin \omega_0 = \sin \frac{\pi}{12}$ or $\sin \omega_1 = \sin \frac{5\pi}{12}$, in the free spectrum Eq. (45). At these points we also found a sizeable degeneracy of eigenmodes, as well as dips or peaks in the various observables. Remarkably, Fig. 4, center, shows that in the interval between these two points the fractal dimension of bulk modes equals 2 within errors, departing from it outside this interval and dropping towards zero as one enters the low or high mode region. Moreover, in the whole bulk region there is little to no dependence on the lattice volumes used for the estimate of α . This suggests that also in the complex sectors the Anderson transition at the mobility edges is of BKT type.

This picture is again supported by our findings for the spectral statistics (Fig. 4, bottom), which are similar to those obtained in the real sector. The main difference, besides the position of the mobility edges, is the lower value of I_{s_0} attained by the low modes in the complex sectors on the available volumes. This agrees with the fact that in the complex sectors the localized low modes are more extended than in the real sector (see Figs. 3 and 4, top panels). In fact, the typical overlap between two distinct, well localized modes in a finite system is small but nonetheless finite, vanishing only in the infinite-volume limit where they can be arbitrarily far apart. This leads to a finite correlation between the fluctuations of the corresponding eigenvalues under a change in the gauge field configuration, and so to a deviation from Poisson statistics, which in particular shows up as a finite-volume effect in the unfolded level spacing distribution. Clearly, localized modes of larger size have larger typical overlap, and so a larger deviation from Poisson statistics.

c. Near-zero modes The localization properties of the near-zero modes as a function of β are summarized in Fig. 5 (top), where we show the fractal dimension α of modes in the lowest spectral bin $\lambda_n \in [0, \Delta\lambda]$. Central values correspond to α obtained from the pair of largest sizes (28, 32). Error bars are obtained by adding in quadrature the statistical error and the systematic error due to finite-size effects, estimated as the standard deviation of the sample of values of α obtained from all possible pairs of sizes (N_{s1}, N_{s2}) .

A drastic change takes place at the deconfinement transition, both in the real and in the complex sectors, as modes suddenly turn from critical to localized, with a fractal dimension compatible with zero within numerical

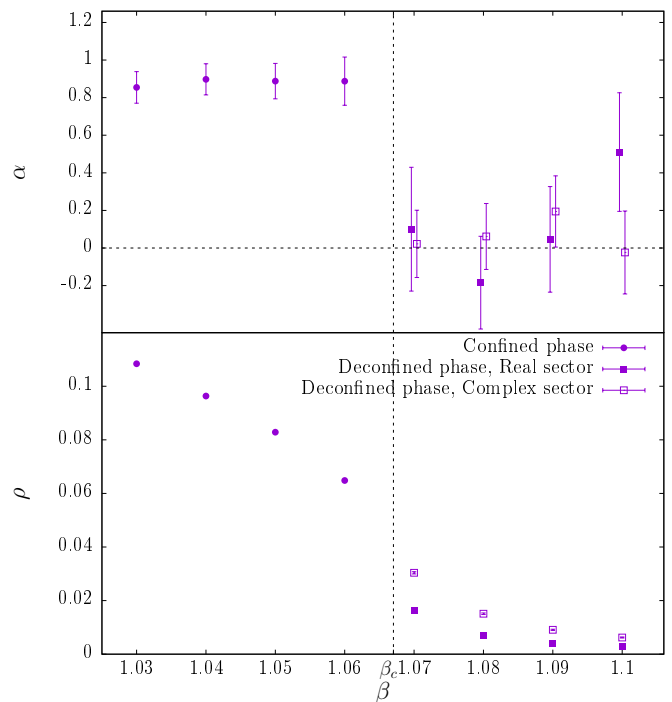


FIG. 5. Top: fractal dimension of near-zero modes as a function of β . Data points for the real and complex sectors in the deconfined phase have been symmetrically shifted horizontally for clarity. Bottom: spectral density of near-zero modes as a function of β . Here $N_s = 32$.

errors. For the real sector this gives further support to the general expectation that localized low modes appear right at the deconfinement transition. For the complex sector this requires instead to revisit the sea-islands picture. Error bars are noticeably larger in the deconfined phase than in the confined phase, both close to β_c and high above it. Close to the transition, this is mostly due to large finite-size effects caused by the correlation length of the system diverging at β_c , causing also a visible increase in the error for the closest point in the confined phase. Another source of uncertainty is the low count of near-zero modes in the deconfined phase, discussed below.

In Fig. 5 (bottom) we show the spectral density of near-zero modes, i.e., the average number of modes per unit volume in the lowest spectral bin divided by $\Delta\lambda$. This decreases with increasing β , changing more rapidly near the transition, and becoming very small although still nonzero at large β . This explains why the error bars for α remain large also far from the transition.

Different values are found in the two center sectors, with a lower density in the real one. These findings are consistent with the quite general pattern of deconfinement improving on the chiral symmetry properties of the system, indicated here by the large decrease in the near-zero spectral density; and with the fact that fermions prefer the real Polyakov-loop sector over the complex ones.

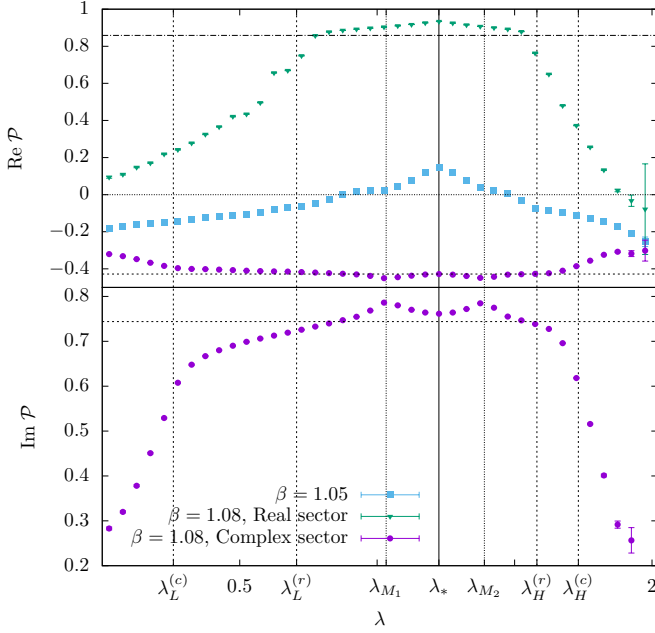


FIG. 6. The real part of the Polyakov loop weighted by the modes (top), and its imaginary part in the deconfined phase in the complex sector $\text{Im } \bar{P} > 0$ (bottom). The horizontal lines correspond to the real or the imaginary part of the average Polyakov loop $\langle P \rangle$, as appropriate, in the deconfined phase – real sector (dot-dashed), confined (short dashed), and deconfined phase – complex sector (long dashed). Here $N_s = 32$.

B. Gauge observables

In Fig. 6 we show our results for the correlation between eigenmodes and Polyakov loops. For bulk modes, $\text{Re } \bar{P}$ is always close to the real part of the expectation value $\langle \text{Re } P \rangle$ of the Polyakov loop. In the confined phase ($\langle P \rangle = 0$) and in the deconfined phase in the real sector ($\langle \text{Re } P \rangle > 0$) there is a mild correlation with real Polyakov loops, while in the deconfined phase in the complex sectors ($\langle \text{Re } P \rangle < 0$) the deviation from $\langle \text{Re } P \rangle$ is minimal. For low and high modes, the behavior of $\text{Re } \bar{P}$ is quite different in the three cases. In the confined phase $\text{Re } \bar{P}$ shows a mild correlation of the eigenmodes with complex Polyakov loops. In the deconfined phase in the real sector $\text{Re } \bar{P}$ shows a strong correlation of the eigenmodes with complex Polyakov loops, with $\text{Re } \bar{P}$ reaching down to almost 0 for low modes, and to negative values for high modes. This means that around 2/3 or more of the weight of the low modes is found on islands of Polyakov-loop fluctuations. This agrees with the standard sea-islands picture, as there are very few islands of fluctuations and still a large fraction of the mode is localized on those islands.

On the other hand, in the deconfined phase in the complex sectors $\text{Im } \bar{P}$ shows a strong correlation of these modes with Polyakov-loop fluctuations in the opposite complex sector, and moreover $\text{Re } \bar{P}$ shows a mild but sizeable correlation with real Polyakov-loop fluctuations.

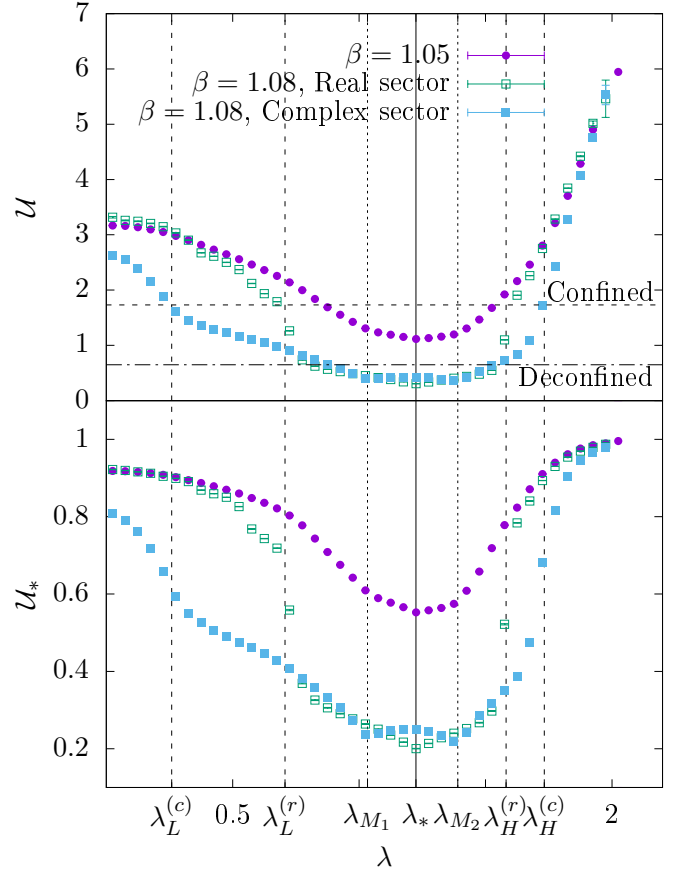


FIG. 7. Average number of non-trivial plaquettes touched by a mode (top), and weight of modes on negative plaquettes (bottom). Horizontal lines in the top panel correspond to $8\langle 1 - U_{\mu\nu} \rangle$ at the given β values in the confined and deconfined phase. Here $N_s = 32$.

This means that the localized low and high modes have larger weight on Polyakov-loop fluctuations than delocalized modes, including on the “energetically unfavorable” real Polyakov-loop fluctuations, which for the low modes contradicts the general expectations of the standard sea-islands picture.

In Fig. 7 we show our results for the correlation between eigenmodes and nontrivial plaquettes. Qualitatively, the situation is the same found for \mathbb{Z}_2 gauge theory [12]. Low and high modes always show a strong correlation with nontrivial plaquettes, as signalled by a value of \bar{U}_* close to 1; and with clusters of nontrivial plaquettes in particular, as signalled by a value of \bar{U} larger than 1. For the low modes this happens independently of their localization properties, although in the deconfined phase, where nontrivial plaquettes become less frequent, this indicates localization. For modes deep in the bulk (near λ_*) one finds instead a value of \bar{U} close to (and below) the value $8\langle 1 - U_{\mu\nu} \rangle$ expected for perfectly delocalized modes ($|\psi|^2 = 1/(N_t V)$). The correlation with clusters of nontrivial plaquettes generally increases as one moves away from the deep bulk near λ_* , where modes are repelled

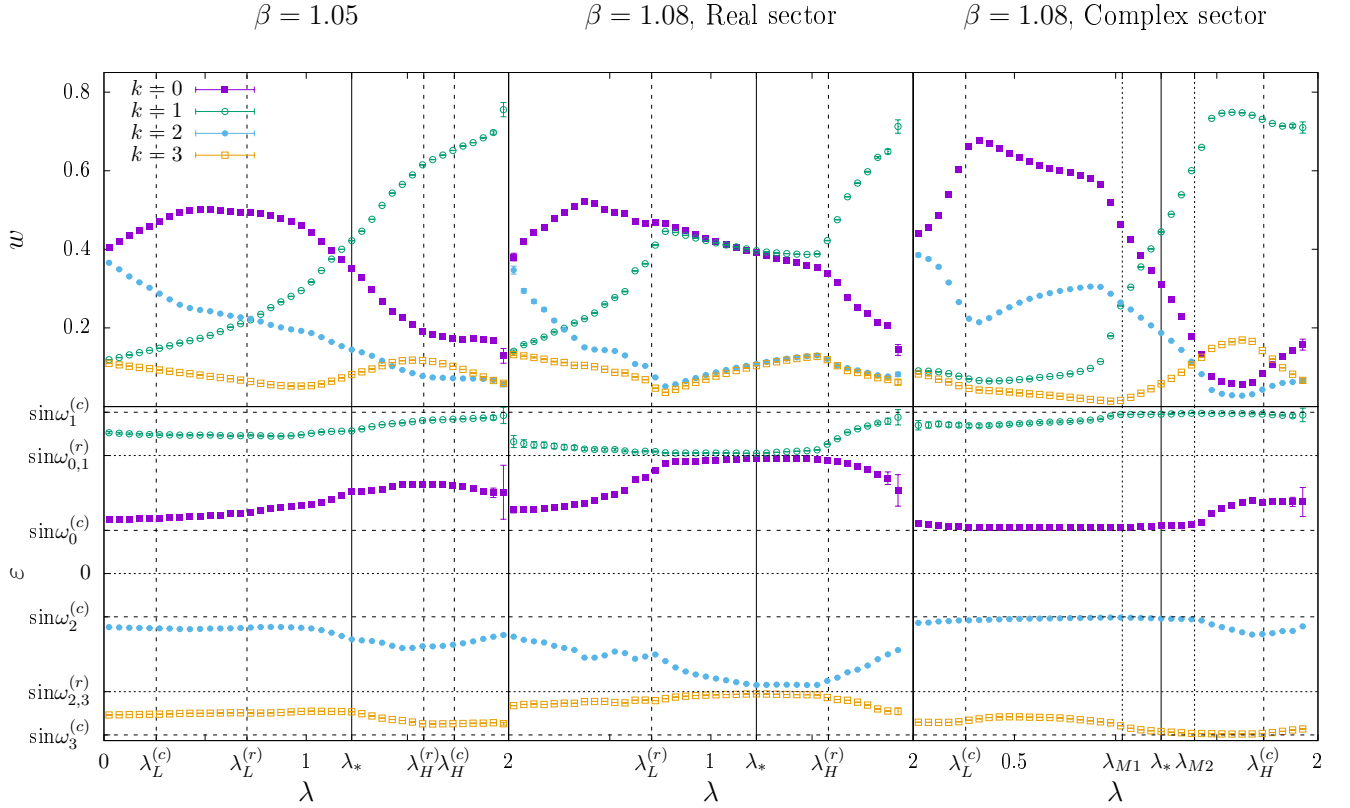


FIG. 8. Standard sea-islands picture: average weight (top row) and energy (bottom row) per branch, in the confined phase (left panels), deconfined phase – real sector (center panels), and deconfined phase – complex sectors (right panels). Here $N_s = 20$ and $N_t = 4$.

by them. The mode weight on negative plaquettes keeps similarly increasing as one moves away from λ_* . Notably, in the deconfined phase the special points in the spectrum correspond to clear changes in the behavior of \overline{U} and \overline{U}_* .

C. Standard sea-islands picture

To study the standard sea-islands picture in detail, we measured the weights and average energy of the various branches of the eigenmodes, Eqs. (37) and (38), averaged locally in the spectrum, Eq. (16). For the confined phase we chose $\beta = 1.05$, while for the deconfined phase we chose $\beta = 1.08$ and looked at the real sector and at the complex sector with $\text{Im } \bar{P} > 0$. For each setup we used 100 configurations on a $20^2 \times 4$ lattice. Our results are shown in Fig. 8. Irrespectively of the phase or center sector, the lowest positive modes have the largest weight on the $k = 0$ branch, as expected, but also a sizeable weight on the corresponding negative branch $k = \frac{N_t}{2} = 2$, up to (and also partially including, for the confined phase and the complex sectors in the deconfined phase) the bulk region. In the deconfined phase in the real sector, $k = 0$ and $k = 1$ have practically equal weights throughout the bulk. This can be understood by noticing that these two branches are degenerate for $\phi(\vec{x}) = 0$, so that for

bulk modes, delocalized all over the sea of ordered and trivial Polyakov loops, one expects that they fully mix. This kind of degeneracy between branches is generally expected in the real sector, since for $\phi(\vec{x}) = 0$ one finds $\sin \tilde{\omega}_{\frac{N_t}{2}-1-k}(0) = \sin \tilde{\omega}_k(0)$. The same argument applies to the pair of branches $k = 1, 3$. The branch $k = N_t - 1 = 3$ never contributes substantially to the eigenmodes, except at the high end of the bulk in the deconfined phase in the complex sectors, where it gives the second largest contribution.

Except for the large mixing of branches in the bulk of the spectrum observed in the deconfined phase in the real sector, whose origin is clear, our results show that in the bulk and in the high-energy regions there is always one of the coupled Anderson models dominating the wave function (except of course in the transition regions where the dominant Anderson model changes). For the lowest modes, instead, the $k = 0$ (positive) and the $k = \frac{N_t}{2} = 2$ (negative) branch contribute comparably. This requires only a rather mild adjustment to the expectations of the standard sea-islands picture, with the positive and the negative energy level closest to zero both playing a role. Nonetheless, this does not help explaining why low modes localize in the complex Polyakov-loops sectors.

Results for the average energy level seen by a branch are again in nice agreement with the standard expect-

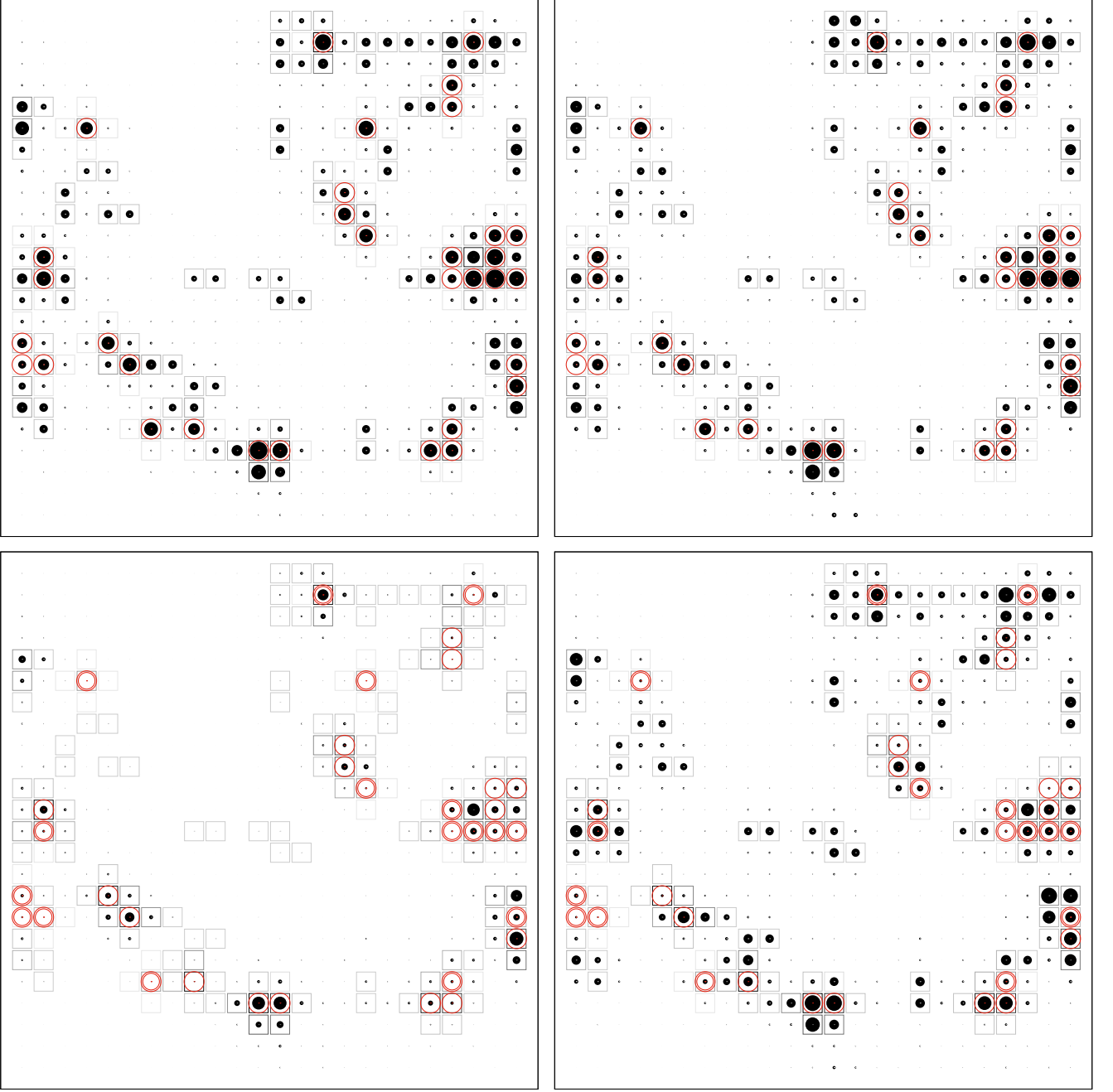


FIG. 9. Correlation between mode amplitude and hopping terms for a single $32^2 \times 4$ gauge configuration at $\beta = 1.08$ (top row), and for its center-rotated version in the complex sector $\text{Im } \bar{P} > 0$ (bottom row), for low modes ($\lambda_n \leq \lambda_L$, left panels) and high modes ($\lambda_n \geq \lambda_H$, right panels). Dots are located on spatial lattice sites, and squares cover the corresponding Wigner-Seitz cell. The dot size is proportional to the low and high mode amplitudes p_L and p_H , Eq. (48), with an extra enhancement factor $5/3$ in the complex sector for better visualization. Red circles denote nontrivial Polyakov loops; in the complex sector, a double circle denotes a real Polyakov loop. A darker shade of gray of the squares corresponds to a larger \mathcal{A} , Eq. (47), indicating a more favorable place for localization according to the refined sea-islands picture.

tations in the case of the real sector of the deconfined phase, with the leading $k = 0$ and $k = 2$ branches of the low modes clearly showing a preference for Polyakov-loop fluctuations to the complex sectors. For bulk modes instead one observes an approximate degeneracy of the $k = 0, 1$ and of the $k = 2, 3$ branches, as one would expect

based on the discussion above. In the complex sectors of the deconfined phase, instead, the low localized modes show a small but clear deviation from what one would naïvely expect, indicating again that they are surprisingly favoring real Polyakov-loop fluctuations over the more “energetically” convenient sea. This further calls

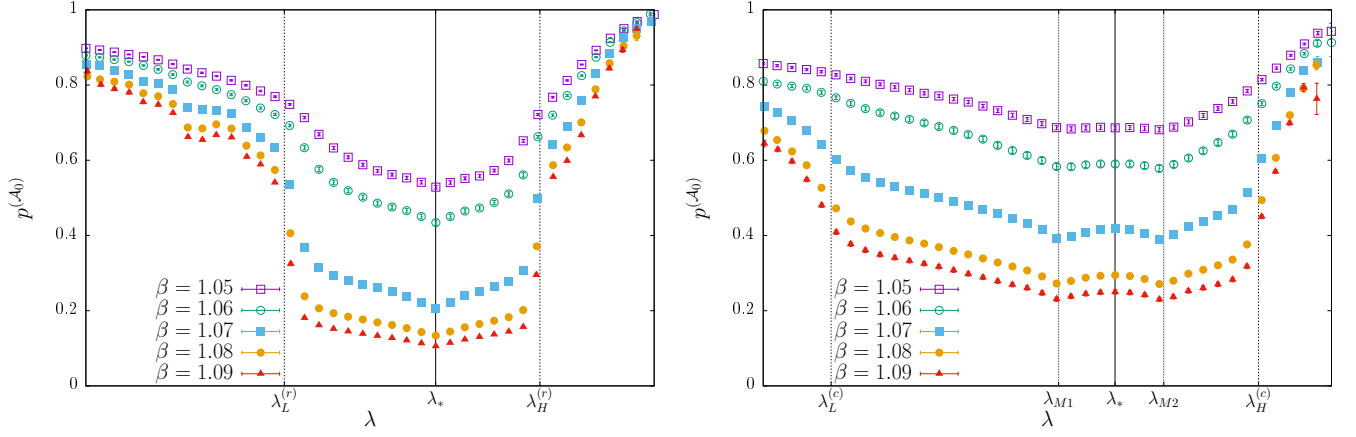


FIG. 10. Average mode weight on sites where $\mathcal{A}(\vec{x}) \geq \mathcal{A}_0$, in the real sector (left) and in the complex sectors (right), on a $32^2 \times 4$ lattice. Here $\mathcal{A}_0 = 1/16$.

for reconsidering the standard sea-islands picture.

D. Refined sea-islands picture

To test the refined sea-islands picture discussed in Sec. IV C, we have directly inspected a few gauge configurations in the deconfined phase, both in the real and in the complex Polyakov-loop sectors, looking for correlations between where localized modes live and the locations where the hopping terms deviate from $A_j \approx 0$. As a measure of this deviation we used

$$\mathcal{A}(\vec{x}) = \frac{1}{8} \sum_{j=1}^2 \text{tr} \{ A_j(\vec{x})^\dagger A_j(\vec{x}) + A_j(\vec{x} - \hat{j})^\dagger A_j(\vec{x} - \hat{j}) \}, \quad (47)$$

with $\mathcal{A}(\vec{x}) \in [0, 1]$. To identify where modes localize, we summed their amplitude square over time slices, and over modes in the low ($0 \leq \lambda_n \leq \lambda_L$) and high ($\lambda_n \geq \lambda_H$) spectral regions,

$$p_L(\vec{x}) = \left\langle \sum_{0 \leq \lambda_n \leq \lambda_L} \sum_{t=0}^{N_t-1} |\psi_n(\vec{x}, t)|^2 \right\rangle, \quad (48)$$

$$p_H(\vec{x}) = \left\langle \sum_{\lambda_n \geq \lambda_H} \sum_{t=0}^{N_t-1} |\psi_n(\vec{x}, t)|^2 \right\rangle,$$

with $\lambda_{L,H}$ depending on the center sector under study. Results are shown in Fig. 9 for one typical configuration in the real sector and its center-rotated version in the complex sector $\text{Im } \bar{P} > 0$. The correlation between larger \mathcal{A} and localization is clear in both center sectors. In the real sector, regions with \mathcal{A} deviating from zero cover the areas favorable for localization much more accurately than fluctuations of the Polyakov loop to the complex sector. In particular, regions where modes do indeed localize but far from Polyakov-loop fluctuations are correctly identified by using $\mathcal{A} \approx 0$ as a criterion. In the complex

sector, where the standard sea-islands picture leads one to expect delocalized low modes, $\mathcal{A} \approx 0$ again correctly identifies locations where both low and high modes localize. These include also sites where the Polyakov loop fluctuates to the real sector, which the standard sea-islands picture would deem “energetically” unfavorable. Notice that on these configurations \mathcal{A} reaches up at most to around 0.42 in the real sector and to around 0.47 in the complex sector.

To see how modes in different spectral regions respond to fluctuations in the spatial hopping terms, as measured by $\mathcal{A}(\vec{x})$, we have measured the mode weight on sites where this is above a fixed tolerance level,

$$p_n^{(\mathcal{A}_0)} = \sum_{\vec{x}} \sum_{t=0}^{N_t-1} \theta(\mathcal{A}(\vec{x}) - \mathcal{A}_0) |\psi_n(\vec{x}, t)|^2, \quad (49)$$

and averaged it locally in the spectrum according to Eq. (16). We analyzed separately configurations in the real and complex Polyakov-loop sectors, also in the confined phase where the difference should be milder. Results are shown in Fig. 10, using $\mathcal{A}_0 = 1/16$. Since the volume dependence is rather mild, only data for $N_s = 32$ are shown. We used 200 configurations for each β value. Low and high modes favor regions with larger $\mathcal{A}(\vec{x})$ in all phases and center sectors. In the real sector of the deconfined phase, $\bar{p}^{(\mathcal{A}_0)}(\lambda)$ changes abruptly when entering the bulk, where it drops by a factor of 2 or more. In the complex sector the decrease is smoother, but a change in behavior is clearly visible, and a significant drop is found comparing the lowest modes with the bulk modes. Since in the deconfined phase sites with $\mathcal{A}(\vec{x}) \approx 0$ become less frequent, low modes favoring them comes at the price of becoming localized.

These results strongly support the refined sea-islands picture discussed in Sec. IV C, which allows one to explain the observed localization of low modes in the complex Polyakov-loop sectors. This also partially explains the strong correlation between localized modes and nontrivial plaquettes displayed in Fig. 7. Indeed, nontrivial

spatial-temporal plaquettes indicate the presence of the kind of disorder in the hopping terms that, as argued above, leads to favorable locations for localized low (as well as high) modes.

VII. CONCLUSIONS

Localized low Dirac modes are found in the deconfined phase of many gauge theories and related models [1–23], appearing precisely at deconfinement when this is a genuine phase transition [2–14]. This naturally suggests a close connection between low-mode localization and deconfinement. An explanation of this connection is provided by the sea-islands picture of localization [1, 7, 20–22], according to which islands of fluctuations in the sea of ordered Polyakov loops found in the deconfined phase provide favorable locations for Dirac eigenmodes, as they effectively and locally reduce the twist on the fermion wave functions induced by the antiperiodic temporal boundary conditions. A prediction of the sea-islands picture is then that the low-lying Dirac modes become localized in the deconfined phase of a gauge theory, under quite general conditions. So far, this prediction has always been successfully verified. Moreover, numerical support for the proposed mechanism has been provided [7, 12, 18, 19].

In this paper we have studied the localization properties of the eigenmodes of the staggered lattice Dirac operator in 2+1 dimensional \mathbb{Z}_3 pure gauge theory. This model provides nontrivial tests for the standard sea-islands picture of localization outlined above. In the deconfined phase in the physical, real Polyakov-loop sector where the Polyakov loop gets ordered near $P(\vec{x}) = 1$, fluctuations to the complex sectors $P(\vec{x}) = e^{\pm i\frac{2\pi}{3}}$ provide only a mild gain in twist, and low modes may not be able to localize. More importantly, in the complex Polyakov-loop sectors where $P(\vec{x})$ gets ordered near $e^{i\frac{2\pi}{3}}$ or $e^{-i\frac{2\pi}{3}}$, local fluctuations provide no gain in twist at all, leaving it unchanged (for fluctuations to the opposite complex sector) or even increasing it (for fluctuations to the real sector). A simple-minded use of the sea-island picture then leads one to expect that low modes do not localize in this case.

Our numerical results show that localized low modes are present in the deconfined phase both in the real and in the complex sectors, appearing right at the deconfinement transition in both cases. While for the real sector our results agree with the general expectations of the standard sea-islands picture, for the complex sector this is unexpected. Even more puzzlingly, in this case the localized low modes do not avoid Polyakov-loop fluctuations to the real sector, as one would expect.

A comprehensive understanding of these results is obtained by reconsidering the sea-islands picture from the point of view of the spatial hopping terms of the Dirac operator, rather than of the Polyakov-loop fluctuations. Hopping terms are strongly influenced by the presence of

Polyakov-loop fluctuations, but quite independently of the gain or loss in the temporal twist on the wave functions that these provide. Moreover, for a strongly ordered configuration of Polyakov loops *and* spatial links, the resulting “ordered-type” hopping terms lead to the opening of a gap in the spectrum and to full delocalization of the eigenmodes; deviations from order modify the hopping terms to “non-ordered-type”, and generally allow for eigenvalues below the gap. Typical configurations in the deconfined phase display a sea of sites connected by ordered-type hopping terms, with rare islands where one or more of the hopping terms is of non-ordered-type. Localizing on these islands allows the mode to penetrate the spectral gap, and so explains localization of the low modes, as well as their low density. In the language of first-order perturbation theory, modes living on islands are stable against delocalization due to the fact that they can hardly mix among themselves, due to large spatial separation, and with delocalized modes living on the sea, due to the large energy difference coming from the presence of a gap.

Islands where hopping terms of non-ordered type are present can also support modes with much larger eigenvalues than those found in the presence of ordered-type hopping terms, and so support localized high modes by a similar no-mixing argument. Even in the confined phase, where no sea is present, particularly favorable fluctuations in the hopping terms supporting very large modes are likely to be spatially separated, and so high modes are again expected to be localized. However, it is only in the deconfined phase where a spectral (pseudo)gap opens that low modes living on islands are stable against delocalization. In the confined phase there is instead no gap and there are no islands, and so no no-mixing argument and no reason for low modes not to delocalize. A simple way to describe the different situations in the two phases is that the ordering of the Polyakov loop and the resulting spectral pseudogap in the deconfined phase makes the near-zero region similar to a spectrum edge with low spectral density. In such a region even a relatively weak disorder (and in gauge theories the disorder strength is bounded due to the unitary nature of link variables) can lead to mode localization, as it is known from the study of Anderson models.

While non-ordered-type islands are expected to correlate strongly with Polyakov-loop fluctuations away from its ordered value, they do not require any gain in temporal twist to become favorable to localization (and can also be found away from any Polyakov-loop fluctuation). This is consistent with the observed correlation between localized modes and Polyakov-loop fluctuations in the physical center sector of the deconfined phase [7, 12, 18, 19]. At the same time, this also explains why low modes can localize even in the complex sectors of \mathbb{Z}_3 gauge theory in the deconfined phase, where no gain in temporal twist can be obtained anywhere.

It is worth noticing that in $SU(3)$ pure gauge theory no localized modes were found in the complex \mathbb{Z}_3 cen-

ter sectors at the critical point [65], while the results of Refs. [2, 3] deeper in the deconfined phase do not allow for conclusive statements. This calls for further investigation of the onset of low-mode localization in a complex center sector of a gauge theory.

While the specific results obtained for \mathbb{Z}_3 are likely to be strongly affected by the discreteness of the gauge group and the lower dimensionality of the system, the refined sea-islands mechanism unveiled here should be of universal value and apply to a general gauge theory. This should be tested on physically more relevant models, including lattice QCD.

ACKNOWLEDGMENTS

We thank M. Caselle and A. Papa for correspondence on the \mathbb{Z}_N models, and T. G. Kovács for discussions and for a careful reading of the manuscript. MG was partially supported by the NKFIH grant KKP-126769.

Appendix A: Duality in 2+1 dimensional \mathbb{Z}_N gauge theories on finite lattices

The partition function of 2+1 dimensional \mathbb{Z}_N gauge theories on a finite $N_1 \times N_2 \times N_3$ cubic lattice Λ can be written as (see Ref. [41])

$$Z = e^{-3\beta\mathcal{V}} \sum_{\{k_p\}} \prod_{\ell} \delta_{C_{\ell},0} \prod_p c_{k_p}(\beta), \quad (\text{A1})$$

where $\mathcal{V} = N_1 N_2 N_3$, and ℓ and p run, respectively, over links and plaquettes, with links conventionally oriented in the same direction as the unit lattice vectors, and plaquettes oriented counterclockwise. The sum over $\{k_p\}$ runs over all choices of the integers $k_p = 0, \dots, N-1$, each associated with a plaquette p . Moreover, c_{k_p} are known coefficients and, for each link ℓ , $\delta_{C_{\ell},0}$ imposes the constraint

$$C_{\ell} = \sum_{\substack{p \\ \ell \in \partial p}} \tau_p k_p = 0 \pmod{N}, \quad (\text{A2})$$

where ∂p is the boundary of plaquette p , and $\tau_p = +1$ or -1 depending on whether one traverses ℓ along or opposite to its orientation when going around p .

The constraints in Eq. (A2) are most easily solved using the dual lattice $\tilde{\Lambda}$, with dual sites located at the center of elementary cubes of the original (direct) lattice. Dual links $\tilde{\ell}$ connecting dual sites pierce exactly one of the direct plaquettes p perpendicularly, and in the same direction as the plaquette orientation. Dual links and direct plaquettes are then identified. In this setup, after setting $\tilde{k}_{\tilde{\ell}} = k_p$, solving Eq. (A2) is equivalent to finding the most general configuration of gauge link variables $V_{\tilde{\ell}} = e^{i\frac{2\pi\tilde{k}_{\tilde{\ell}}}{N}}$ such that for all elementary dual plaquettes

one has $\prod_{\tilde{\ell} \in \partial \tilde{p}} V_{\tilde{\ell}} = 1$. The solution is found by transforming to the maximal temporal gauge (mtg),

$$V_{\tilde{\ell}}^{\text{mtg}} = 1 \text{ for } \tilde{\ell} = \begin{cases} (\tilde{n}, \hat{1}), & 0 \leq \tilde{n}_1 < N_1 - 1; \\ (\tilde{n}, \hat{2}), \tilde{n}_1 = 0, & 0 \leq \tilde{n}_2 < N_2 - 1; \\ (\tilde{n}, \hat{3}), \tilde{n}_{1,2} = 0, & 0 \leq \tilde{n}_3 < N_3 - 1, \end{cases} \quad (\text{A3})$$

where $\tilde{\ell} = (\tilde{n}, \hat{\mu})$ is the dual link connecting \tilde{n} and $\tilde{n} + \hat{\mu}$. For each configuration there are exactly N gauge transformations $G_g(\tilde{n})$, all leading to the same set of new link variables $V_{\tilde{\ell}}^{\text{mtg}}$ satisfying the maximal temporal gauge condition Eq. (A3),

$$V_{\tilde{\ell}} = G_g(\tilde{n}) V_{\tilde{\ell}}^{\text{mtg}} G_g(\tilde{n} + \hat{\mu})^*. \quad (\text{A4})$$

These read $G_g(\tilde{n}) = e^{i\frac{2\pi g}{N}} s(\tilde{n})$, with $g = 0, \dots, N-1$, and $s(\tilde{n}) = e^{i\frac{2\pi\sigma(\tilde{n})}{N}}$, with $\sigma(\tilde{n}) = 0, \dots, N-1$, and

$$s(\tilde{n}) = W_3(0, 0, 0; 0, 0, \tilde{n}_3) \times W_2(0, 0, \tilde{n}_3; 0, \tilde{n}_2, \tilde{n}_3) \times W_1(0, \tilde{n}_2, \tilde{n}_3; \tilde{n}_1, \tilde{n}_2, \tilde{n}_3), \quad (\text{A5})$$

$$W_{\mu}(\tilde{n}; \tilde{n} + L\hat{\mu}) = \prod_{s=0}^{L-1} V_{(\tilde{n}+s\hat{\mu}, \hat{\mu})}^*.$$

In this gauge the solution is readily found and reads

$$V_{\tilde{\ell}}^{\text{mtg}} = 1, \quad \text{if } \tilde{\ell} \notin \cup_{\mu=0}^3 \partial_{\mu} \tilde{\Lambda}, \\ V_{\tilde{\ell}}^{\text{mtg}} = B_{\mu} = e^{i\frac{2\pi b_{\mu}}{N}}, \quad \text{if } \tilde{\ell} \in \partial_{\mu} \tilde{\Lambda}, \quad (\text{A6})$$

with $b_{\mu} = 0, \dots, N-1$, and where

$$\partial_{\mu} \tilde{\Lambda} = \{\tilde{\ell} = (\tilde{n}, \hat{\mu}) \mid \tilde{n}_{\mu} = N_{\mu} - 1\} \quad (\text{A7})$$

denotes the links on the boundary of the dual lattice in direction μ . The value of B_{μ} is the same across the whole boundary $\partial_{\mu} \tilde{\Lambda}$. Undoing the gauge transformation, one writes for the most general solution

$$V_{(\tilde{n}, \hat{\mu})} = e^{i\frac{2\pi\tilde{k}_{(\tilde{n}, \hat{\mu})}}{N}} = s(\tilde{n}) s(\tilde{n} + \hat{\mu})^*, \quad (\text{A8})$$

with arbitrary $s(\tilde{n})$ obeying the boundary condition $s(\tilde{n} + N_{\mu}\hat{\mu}) = B_{\mu} s(\tilde{n})$. Equivalently, one has $\tilde{k}_{(\tilde{n}, \hat{\mu})} = \sigma(\tilde{n}) - \sigma(\tilde{n} + \hat{\mu})$, with arbitrary $\sigma(\tilde{n})$ satisfying the boundary condition $\sigma(\tilde{n} + N_{\mu}\hat{\mu}) = \sigma(\tilde{n}) + b_{\mu} \pmod{N}$. One easily shows that the $V_{(\tilde{n}, \hat{\mu})}$ are uniquely identified by the spin variables $s(\tilde{n})$ or $\sigma(\tilde{n})$ and by the boundary conditions B_{μ} up to global transformations $s(\tilde{n}) \rightarrow s(\tilde{n}) e^{i\frac{2\pi g}{N}}$, $g = 0, \dots, N-1$, corresponding to the N gauge transformations leading to maximal temporal gauge. Summing without restrictions over $s(\tilde{n})$ or $\sigma(\tilde{n})$ and over all possible boundary conditions yields then all the allowed

configurations of $\tilde{k}_{\vec{\ell}}$, with each configuration appearing exactly N times. One concludes that

$$Z = e^{-3\beta V} N^{-1} \sum_{\{b_\mu\}} \tilde{Z}_{\{b_\mu\}},$$

$$\tilde{Z}_{\{b_\mu\}} = \sum_{\{\sigma(\tilde{n})\}} \prod_{(\tilde{n}, \tilde{\mu})} c_{k(\tilde{n}, \tilde{\mu})}(\beta) \Big|_{\substack{k(\tilde{n}, \tilde{\mu}) = \sigma(\tilde{n}) - \sigma(\tilde{n} + \tilde{\mu}) \bmod N, \\ \sigma(\tilde{n} + N_\mu \tilde{\mu}) = \sigma(\tilde{n}) + b_\mu \bmod N}}, \quad (\text{A9})$$

which is the desired duality relation. Substituting the values of $c_k(\beta)$ for $N = 3$ one finds Eq. (3).

Appendix B: Sea-islands picture: technical details

1. Ordering of on-site energies

The ranking of the unperturbed energy levels $e_k(\vec{x}) = \eta_{d+1}(\vec{x}) \sin \omega_k(\vec{x}) = \eta_{d+1}(\vec{x}) \sin \tilde{\omega}_{N_k(\vec{x})}(\phi(\vec{x}))$ by magnitude [see Eqs. (30) and (34)] is achieved by setting $N_k(\vec{x}) = n_k(\phi(\vec{x}), \eta_{d+1}(\vec{x}))$, with $n_k(\phi, \eta_{d+1})$ chosen as follows:

$$\begin{aligned} n_{2k}(\phi, 1) &= \theta_0(-\phi)k + \theta_0(\phi) \left(\frac{N_t}{2} - 1 - k \right), \\ n_{2l+1}(\phi, 1) &= \theta_0(-\phi) \left(\frac{N_t}{2} - 1 - l \right) + \theta_0(\phi)l, \\ n_{2k}(\phi, -1) &= \frac{N_t}{2} + n_{2k}(\phi, 1), \\ n_{2l+1}(\phi, -1) &= \frac{N_t}{2} + n_{2l+1}(\phi, 1), \end{aligned} \quad (\text{B1})$$

with $k, l \in \{0, \dots, \frac{N_t}{4} - 1\}$ if $N_t = 4m$, and $k \in \{0, \dots, \frac{N_t-2}{4}\}$, $l \in \{0, \dots, \frac{N_t-2}{4} - 1\}$ if $N_t = 4m + 2$, and

$$n_{\frac{N_t}{2}+k}(\phi, \pm 1) = \frac{N_t}{2} + n_k(\phi, \pm 1) \bmod N_t, \quad (\text{B2})$$

with $k \in \{0, \dots, \frac{N_t}{2} - 1\}$. Here $\theta_0(x) = 1$ if $x \geq 0$ and $\theta_0(x) = 0$ if $x < 0$.

2. Strongly ordered configurations

For strongly ordered configurations with spatially constant Polyakov loop, $P(\vec{x}) = P_* = e^{i\phi_*}$, the quantity $\omega_k(\vec{x}) = \tilde{\omega}_{n_k(\phi_*, \eta_{d+1}(\vec{x}))}(\phi_*) \equiv \tilde{\omega}_{\hat{n}_k(\eta_{d+1}(\vec{x}))}$ depends on \vec{x} only through the η_{d+1} dependence of n_k , and so only on whether \vec{x} is an even or odd site ($\eta_{d+1} = \pm 1$). Moreover, from Eqs. (B1) and (B2) one has

$$\hat{n}_k(\pm 1) = \frac{N_t}{2} + \hat{n}_k(\mp 1) \bmod N_t. \quad (\text{B3})$$

If also $U_{\pm j}^{\text{tg}}(\vec{x}, t) = U_{\pm j*}^{\text{tg}}(\vec{x})$, as one would approximately expect when there are strong temporal correlations and spatial-temporal plaquettes ($\mu = j$, $\nu = d+1$) reduce to $U_{j\,d+1}(\vec{x}, t) \approx U_j(\vec{x}, t)U_j(\vec{x}, t+1)^*$, then from Eqs. (29),

(30) and (B3) one finds

$$\begin{aligned} V_{\pm j}(\vec{x})_{kl} &= U_{\pm j*}^{\text{tg}}(\vec{x}) \\ &\times \frac{1}{N_t} \sum_{t=0}^{N_t-1} e^{-i \frac{2\pi}{N_t} (\hat{n}_k(\eta_{d+1}(\vec{x})) - \hat{n}_l(\eta_{d+1}(\vec{x})) - \frac{N_t}{2})t} \\ &= U_{\pm j*}^{\text{tg}}(\vec{x}) \delta_{k, l + \frac{N_t}{2} \bmod N_t}. \end{aligned} \quad (\text{B4})$$

If a perfect anticorrelation was found for the spatial links, $U_{\pm j}^{\text{tg}}(\vec{x}, t) = (-1)^t U_{\pm j*}^{\text{tg}}(\vec{x}) = e^{i\pi t} U_{\pm j*}^{\text{tg}}(\vec{x})$, then

$$\begin{aligned} V_{\pm j}(\vec{x})_{kl} &= U_{\pm j*}^{\text{tg}}(\vec{x}) \\ &\times \frac{1}{N_t} \sum_{t=0}^{N_t-1} e^{-i \frac{2\pi}{N_t} (\hat{n}_k(\eta_{d+1}(\vec{x})) - \hat{n}_l(\eta_{d+1}(\vec{x})))t} \\ &= U_{\pm j*}^{\text{tg}}(\vec{x}) \delta_{k, l}. \end{aligned} \quad (\text{B5})$$

These results differs from those reported in Ref. [21] due to the different convention used in defining $\omega_k(\vec{x})$, in particular the inclusion of η_{d+1} in the quantities to be ranked.

3. Non-Abelian case

Here we extend the argument of Sec. IV C to a non-Abelian theory, with link variables $U_\mu(n)$ providing a unitary representation of the gauge group (assumed to be semisimple and compact). In this case the unperturbed eigenvalues $e_{ka}(\vec{x})$ have a further index $a = 1, \dots, N_c$, running over the internal “color” degree of freedom, and are obtained as

$$\begin{aligned} e_{ka}(\vec{x}) &= \eta_{d+1}(\vec{x}) \sin \omega_{ka}(\vec{x}), \\ \omega_{ka}(\vec{x}) &= \tilde{\omega}_{N_{ka}(\vec{x})}(\phi_a(\vec{x})), \end{aligned} \quad (\text{B6})$$

with $\phi_a(\vec{x}) \in [-\pi, \pi)$ the N_c eigenphases of the Polyakov loop

$$\begin{aligned} P(\vec{x}) &= u(\vec{x})^\dagger \text{diag}(e^{i\phi_1(\vec{x})}, \dots, e^{i\phi_{N_c}(\vec{x})}) u(\vec{x}), \\ u(\vec{x})^\dagger u(\vec{x}) &= \mathbf{1}. \end{aligned} \quad (\text{B7})$$

Notice that with our convention one generally finds for special unitary $U_\mu(n)$ that $\sum_{a=1}^{N_c} \phi_a = 2\pi q$ with integer but not necessarily zero q . This differs from the choice made in Ref. [21]. The hopping matrices also acquire extra indices, $V_{\pm j}(\vec{x})_{k a l b}$, and are now defined as

$$\begin{aligned} V_{\pm j}(\vec{x})_{k a l b} &= \frac{1}{N_t} \sum_{t=0}^{N_t-1} e^{-i[\omega_{ka}(\vec{x}) - \omega_{lb}(\vec{x} \pm \hat{j})]t} [U_{\pm j}^{\text{tdg}}(\vec{x}, t)]_{ab}, \\ U_{\pm j}^{\text{tdg}}(\vec{x}, t) &= P(\vec{x}, t) U_{\pm j}(\vec{x}, t) P(\vec{x} \pm \hat{j}, t)^\dagger, \end{aligned} \quad (\text{B8})$$

where $P(\vec{x}, t+1) = P(\vec{x}, t) U_{d+1}(\vec{x}, t)$, $P(\vec{x}, 0) = \mathbf{1}$ is the N_c -dimensional identity matrix, $P(\vec{x}, N_t) = P(\vec{x})$, and moreover $U_{-j}(\vec{x}, t) = U_j(\vec{x} - \hat{j}, t)^\dagger$. Here “tdg” denotes the temporal diagonal gauge where $U_{d+1}^{\text{tdg}}(\vec{x}, t) = \mathbf{1}$, $\forall \vec{x}$,

$0 \leq t < N_t - 1$, and all Polyakov loops are diagonal, $P^{\text{tdg}}(\vec{x}) = \text{diag}(e^{i\phi_a(\vec{x})})$. Notice that $V_{\pm j}(\vec{x})$ are now unitary matrices in the extended $N_c N_t$ -dimensional space. As long as $N_{ka}(\vec{x})$ is chosen so that Eq. (31) holds for all

a , i.e., $e_{k+\frac{N_t}{2} \bmod N_t a}(\vec{x}) = -e_{ka}(\vec{x})$, and that $e_{ka}(\vec{x}) \geq 0$ for $k = 0, \dots, \frac{N_t}{2} - 1$, then Eq. (33) holds, and the argument outlined in Section IV C carries through.

-
- [1] M. Giordano and T. G. Kovács, *Universe* **7**, 194 (2021), arXiv:2104.14388 [hep-lat].
 - [2] M. Göckeler, P. E. L. Rakow, A. Schäfer, W. Söldner, and T. Wettig, *Phys. Rev. Lett.* **87**, 042001 (2001), arXiv:hep-lat/0103031 [hep-lat].
 - [3] C. Gatttringer, M. Göckeler, P. E. L. Rakow, S. Schaefer, and A. Schäfer, *Nucl. Phys. B* **618**, 205 (2001), arXiv:hep-lat/0105023 [hep-lat].
 - [4] R. V. Gavai, S. Gupta, and R. Lacaze, *Phys. Rev. D* **77**, 114506 (2008), arXiv:0803.0182 [hep-lat].
 - [5] T. G. Kovács, *Phys. Rev. Lett.* **104**, 031601 (2010), arXiv:0906.5373 [hep-lat].
 - [6] T. G. Kovács and F. Pittler, *Phys. Rev. Lett.* **105**, 192001 (2010), arXiv:1006.1205 [hep-lat].
 - [7] F. Bruckmann, T. G. Kovács, and S. Schierenberg, *Phys. Rev. D* **84**, 034505 (2011), arXiv:1105.5336 [hep-lat].
 - [8] T. G. Kovács and R. Á. Vig, *Phys. Rev. D* **97**, 014502 (2018), arXiv:1706.03562 [hep-lat].
 - [9] M. Giordano, *J. High Energy Phys.* **05**, 204 (2019), arXiv:1903.04983 [hep-lat].
 - [10] R. Á. Vig and T. G. Kovács, *Phys. Rev. D* **101**, 094511 (2020), arXiv:2001.06872 [hep-lat].
 - [11] C. Bonati, M. Cardinali, M. D'Elia, M. Giordano, and F. Mazzioti, *Phys. Rev. D* **103**, 034506 (2021), arXiv:2012.13246 [hep-lat].
 - [12] G. Baranka and M. Giordano, *Phys. Rev. D* **104**, 054513 (2021), arXiv:2104.03779 [hep-lat].
 - [13] M. Giordano, S. D. Katz, T. G. Kovács, and F. Pittler, *J. High Energy Phys.* **02**, 055 (2017), arXiv:1611.03284 [hep-lat].
 - [14] M. Cardinali, M. D'Elia, F. Garosi, and M. Giordano, *Phys. Rev. D* **105**, 014506 (2022), arXiv:2110.10029 [hep-lat].
 - [15] A. M. García-García and J. C. Osborn, *Phys. Rev. D* **75**, 034503 (2007), arXiv:hep-lat/0611019 [hep-lat].
 - [16] T. G. Kovács and F. Pittler, *Phys. Rev. D* **86**, 114515 (2012), arXiv:1208.3475 [hep-lat].
 - [17] V. Dick, F. Karsch, E. Laermann, S. Mukherjee, and S. Sharma, *Phys. Rev. D* **91**, 094504 (2015), arXiv:1502.06190 [hep-lat].
 - [18] G. Cossu and S. Hashimoto, *J. High Energy Phys.* **06**, 056 (2016), arXiv:1604.00768 [hep-lat].
 - [19] L. Holicki, E.-M. Ilgenfritz, and L. von Smekal, *PoS LATTICE2018*, 180 (2018), arXiv:1810.01130 [hep-lat].
 - [20] M. Giordano, T. G. Kovács, and F. Pittler, *J. High Energy Phys.* **04**, 112 (2015), arXiv:1502.02532 [hep-lat].
 - [21] M. Giordano, T. G. Kovács, and F. Pittler, *J. High Energy Phys.* **06**, 007 (2016), arXiv:1603.09548 [hep-lat].
 - [22] M. Giordano, T. G. Kovács, and F. Pittler, *Phys. Rev. D* **95**, 074503 (2017), arXiv:1612.05059 [hep-lat].
 - [23] F. Bruckmann and J. Wellenhofer, *EPJ Web Conf.* **175**, 07005 (2018), arXiv:1710.05662 [hep-lat].
 - [24] D. Diakonov, *Proc. Int. Sch. Phys. Fermi* **130**, 397 (1996), arXiv:hep-ph/9602375 [hep-ph].
 - [25] A. M. García-García and J. C. Osborn, *Nucl. Phys. A* **770**, 141 (2006), arXiv:hep-lat/0512025 [hep-lat].
 - [26] R. Á. Vig and T. G. Kovács, *Phys. Rev. D* **103**, 114510 (2021), arXiv:2101.01498 [hep-lat].
 - [27] A. Alexandru and I. Horváth, *Phys. Rev. Lett.* **127**, 052303 (2021), arXiv:2103.05607 [hep-lat].
 - [28] A. Alexandru and I. Horváth, *Phys. Lett. B* **833**, 137370 (2022), arXiv:2110.04833 [hep-lat].
 - [29] A. Alexandru and I. Horváth, *Phys. Rev. D* **92**, 045038 (2015), arXiv:1502.07732 [hep-lat].
 - [30] H. T. Ding, S. T. Li, S. Mukherjee, A. Tomiya, X. D. Wang, and Y. Zhang, *Phys. Rev. Lett.* **126**, 082001 (2021), arXiv:2010.14836 [hep-lat].
 - [31] O. Kaczmarek, L. Mazur, and S. Sharma, *Phys. Rev. D* **104**, 094518 (2021), arXiv:2102.06136 [hep-lat].
 - [32] M. Giordano, *J. Phys. A* **54**, 37LT01 (2021), arXiv:2009.00486 [hep-th].
 - [33] M. Giordano, *PoS LATTICE2021*, 401 (2022), arXiv:2110.12250 [hep-lat].
 - [34] M. Giordano, arXiv:2206.11109 [hep-th] (2022).
 - [35] T. G. Kovács and R. A. Vig, *PoS LATTICE2018*, 258 (2019), arXiv:1901.00661 [hep-lat].
 - [36] M. Caselle and M. Hasenbusch, *Nucl. Phys. B* **470**, 435 (1996), arXiv:hep-lat/9511015 [hep-lat].
 - [37] O. Borisenko, V. Chelnokov, G. Cortese, R. Fiore, M. Gravina, and A. Papa, *Phys. Rev. E* **85**, 021114 (2012), arXiv:1112.3604 [hep-lat].
 - [38] O. Borisenko, V. Chelnokov, G. Cortese, R. Fiore, M. Gravina, A. Papa, and I. Surzhikov, *Phys. Rev. E* **86**, 051131 (2012), arXiv:1206.5607 [hep-lat].

- [39] O. Borisenko, V. Chelnokov, G. Cortese, M. Gravina, A. Papa, and I. Surzhikov, Nucl. Phys. B **870**, 159 (2013), arXiv:1212.3198 [hep-lat].
- [40] O. Borisenko, V. Chelnokov, M. Gravina, and A. Papa, Nucl. Phys. B **888**, 52 (2014), arXiv:1408.2780 [hep-lat].
- [41] A. Wipf, *Statistical approach to quantum field theory: An introduction*, Vol. 864 (Springer-Verlag, Berlin Heidelberg, 2013).
- [42] R. H. Swendsen and J.-S. Wang, Phys. Rev. Lett. **58**, 86 (1987).
- [43] U. Wolff, Phys. Rev. Lett. **62**, 361 (1989).
- [44] M. Suzuki, Prog. Theor. Phys. **37**, 770 (1967).
- [45] C. Gruber, A. Hintermann, and D. Merlini, *Group analysis of classical lattice systems*, Vol. 60 (Springer-Verlag, Berlin Heidelberg, 1977).
- [46] M. Caselle, M. Hasenbusch, P. Provero, and K. Zarembo, Nucl. Phys. B **623**, 474 (2002), arXiv:hep-th/0103130 [hep-th].
- [47] L. von Smekal, Nucl. Phys. B Proc. Suppl. **228**, 179 (2012), arXiv:1205.4205 [hep-ph].
- [48] F. Y. Wu, Rev. Mod. Phys. **54**, 235 (1982), [Erratum: Rev. Mod. Phys. **55**, 315 (1983)].
- [49] K. Binder, Z. Phys. B **43**, 119 (1981).
- [50] P. A. Lee and T. V. Ramakrishnan, Rev. Mod. Phys. **57**, 287 (1985).
- [51] F. Evers and A. D. Mirlin, Rev. Mod. Phys. **80**, 1355 (2008), arXiv:0707.4378 [cond-mat.mes-hall].
- [52] B. L. Altshuler and B. I. Shklovskii, Sov. Phys. JETP **64**, 127 (1986).
- [53] M. L. Mehta, *Random matrices*, 3rd ed., Vol. 142 (Elsevier, 2004).
- [54] M. Giordano, T. G. Kovács, and F. Pittler, Phys. Rev. Lett. **112**, 102002 (2014), arXiv:1312.1179 [hep-lat].
- [55] Y.-Y. Zhang, J. Hu, B. A. Bernevig, X. R. Wang, X. C. Xie, and W. M. Liu, Phys. Rev. Lett. **102**, 106401 (2009), arXiv:0810.1996 [cond-mat.dis-nn].
- [56] X. C. Xie, X. R. Wang, and D. Z. Liu, Phys. Rev. Lett. **80**, 3563 (1998).
- [57] M. R. Zirnbauer, Nucl. Phys. B **941**, 458 (2019), arXiv:1805.12555 [math-ph].
- [58] E. J. Dresselhaus, B. Sbierski, and I. A. Gruzberg, Ann. Phys. (Amsterdam) **431**, 168560 (2021), arXiv:2101.01716 [cond-mat.dis-nn].
- [59] G. P. Lepage, B. Clark, C. T. H. Davies, K. Hornbostel, P. B. Mackenzie, C. Morningstar, and H. Trotter, Nucl. Phys. B Proc. Suppl. **106**, 12 (2002), arXiv:hep-lat/0110175 [hep-lat].
- [60] F. James and M. Roos, Comput. Phys. Commun. **10**, 343 (1975).
- [61] F. James, MINUIT Function Minimization and Error Analysis: Reference Manual Version 94.1 (1994).
- [62] V. Beffara and H. Duminil-Copin, Probab. Theory Relat. Fields **153**, 511 (2012), arXiv:1006.5073 [math.PR].
- [63] T. Tomé and A. Petri, J. Phys. A **35**, 5379 (2002), arXiv:cond-mat/0205592 [cond-mat.stat-mech].
- [64] E. Anderson, Z. Bai, C. Bischof, S. Blackford, J. Demmel, J. Dongarra, J. Du Croz, A. Greenbaum, S. Hammarling, A. McKenney, and D. Sorensen, *LAPACK Users' Guide* (SIAM, Philadelphia, 1999).
- [65] T. G. Kovács, PoS LATTICE2021, 238 (2022), arXiv:2112.05454 [hep-lat].